Human Molecular Genetics, 2012, Vol. 21, No. 6 ***1230–1247***
doi:10.1093/hmg/ddr554
Advance Access published on November 23, 2011

A TAT–Frataxin fusion protein increases lifespan and cardiac function in a conditional Friedreich's ataxia mouse model

Piyush M. Vyas[1], Wendy J. Tomamichel[1], P. Melanie Pride[1], Clifford M. Babbey[1], Qiujuan Wang[1], Jennifer Mercier[2], Elizabeth M. Martin[1] and R. Mark Payne[1,*]

[1]Riley Heart Research Center, Wells Center for Pediatric Research, Indiana University School of Medicine, Indianapolis, IN 46202, USA, [2]Wake Forest University School of Medicine, Winston-Salem, NC 27157, USA

Received October 18, 2011; Revised and Accepted November 21, 2011

Friedreich's ataxia (FRDA) is the most common inherited human ataxia and results from a deficiency of the mitochondrial protein, frataxin (FXN), which is encoded in the nucleus. This deficiency is associated with an iron–sulfur (Fe–S) cluster enzyme deficit leading to progressive ataxia and a frequently fatal cardiomyopathy. There is no cure. To determine whether exogenous replacement of the missing FXN protein in mitochondria would repair the defect, we used the transactivator of transcription (TAT) protein transduction domain to deliver human FXN protein to mitochondria in both cultured patient cells and a severe mouse model of FRDA. A TAT–FXN fusion protein bound iron *in vitro*, transduced into mitochondria of FRDA deficient fibroblasts and reduced caspase-3 activation in response to an exogenous iron-oxidant stress. Injection of TAT–FXN protein into mice with a conditional loss of FXN increased their growth velocity and mean lifespan by 53% increased their mean heart rate and cardiac output, increased activity of aconitase and reversed abnormal mitochondrial proliferation and ultrastructure in heart. These results show that a cell-penetrant peptide is capable of delivering a functional mitochondrial protein *in vivo* to rescue a very severe disease phenotype, and present the possibility of TAT–FXN as a protein replacement therapy.

INTRODUCTION

Friedreich's ataxia (FRDA; OMIM 229300) is a relentlessly progressive cardiac and neurodegenerative disease typically beginning in childhood that leads to loss of motor skills and, ultimately, inability to stand or walk within 10–15 years of onset (1). Virtually all patients develop a cardiomyopathy and heart failure is the most common cause of death (2,3). The prevalence of FRDA is ~1 in 50 000 people with equal frequency in males and females (4), and a carrier frequency of 1:60 to 1:120 (5–8). Inheritance is autosomal recessive and predominantly caused by a GAA triplet expansion in the first intron of the human frataxin (*FXN*) gene on chromosome 9q13–q21.11 (reviewed in 9,10). This triplet expansion, which often exceeds 800 repeats, is predicted to cause the formation of a triple-stranded DNA helix (11) leading to transcriptional inhibition and partial silencing of the FRDA locus with loss of FXN protein expression (12). Additionally, GAA triplet expansions may trigger chromatin condensation making the affected region of genomic DNA transcriptionally inactive (13). There is a correlation between the GAA repeat number and the onset and severity of clinical symptoms with higher repeat numbers being associated with earlier onset and more rapid rate of disease progression (14,15).

FXN is an essential and highly conserved protein expressed in most eukaryotic organisms that appears to function in mitochondrial iron homeostasis, notably the *de novo* biosynthesis of iron–sulfur (Fe–S) cluster proteins (16) and heme biosynthesis (17,18). FXN has been shown to bind iron along an acid ridge and the binding affinity can be significant (19). The exact function of FXN has not been defined but recent studies suggest that FXN functions as an allosteric activator with Fe^{2+} for Fe–S cluster biosynthesis by forming a four-protein complex that includes ISD11, ISCU, FXN and NFS1 (20–22). In this model, FXN induces a conformational change in the

*To whom correspondence should be addressed at: Riley Hospital for Children, Wells Center for Pediatric Research, 1044 West Walnut, R4366, Indianapolis, IN 46202, USA. Tel: +1 3172786239; Fax: +1 3172789298; Email: rpayne@iupui.edu

complex, enabling the direct sulfur transfer from cysteine for the Fe–S cluster assembly. The absence of FXN is associated with a loss of activity in Fe–S-containing proteins (23), such as aconitase, and a loss of energy production (24,25).

The 210 amino acid precursor FXN protein (23.1 kDa) contains an 80 amino acid mitochondrial targeting sequence (MTS) at the amino terminus. It is processed in two steps by the mitochondrial matrix processing peptidase (MPP) (26) as it is imported into the matrix (27). The intermediate form of FXN is cleaved at residue 42 by the MPP, and the mature form of FXN has been shown to be cleaved at amino acid 81 yielding a 130 amino acid with a predicted M_r of 14.2 kDa (28,29). Maturation of the precursor FXN occurs within the mitochondrial matrix and no other intra-mitochondrial post-translational modifications have been identified.

Currently, there is no cure for FRDA. Treatment options at present logically include antioxidants and iron chelation (30,31). Although early clinical trials have shown modest biochemical improvement (32), these therapies have not shown substantial clinical improvement as they are designed to control downstream events resulting from the loss of FXN. Using a cell-penetrant peptide, transactivator of transcription (TAT), we tested the hypothesis that a TAT–FXN fusion protein could rescue the phenotype of FRDA using both patient fibroblasts, and extend the lifespan of the severe phenotype of the conditional FXN knockout mouse (33) as functional measures. TAT is a short, cationic peptide capable of efficiently delivering a protein cargo into multiple tissues (34) and organelles, such as a mitochondria (35), lysosomes (36) and the nucleus (37), as well as delivering a fusion protein across the placenta (38). TAT appears to utilize multiple mechanisms to accomplish transduction across cell membranes (39), and two additional recent studies show that enzyme replacement therapy based on TAT-fusion proteins can significantly increase both mitochondrial and cytosolic enzyme activities *in vivo* (40,41). Our data show that a TAT–FXN fusion protein was able to rescue both FRDA patient fibroblast cells, as well as the severe short-lived phenotype of the conditional FXN knockout mouse model with deletion of the *Fxn* gene in cardiac and neural crest-derived tissues. Taken together, these data show that the cell-penetrant peptide, TAT, can deliver a functionally active protein to mitochondria to rescue a severe phenotype in the intact animal. These results suggest that a TAT-based enzyme replacement therapy may be an effective approach for patients with mitochondrial protein defects.

RESULTS

TAT–FXN transduces into mitochondria of FXN-deficient human fibroblasts

The structure of the TAT–FXN fusion protein is shown in Figure 1A. TAT–FXN was expressed and purified from BL21 cells (see Supplementary Material, Fig. S1). To determine whether the TAT–FXN fusion protein would transduce across both cell and mitochondrial membranes, TAT–FXN was labeled with 5-iodoacetamidofluorescein (5-IAF), incubated with FXN-deficient fibroblasts from FRDA patients for 3 h and then removed from the media. At 120 h after exposure

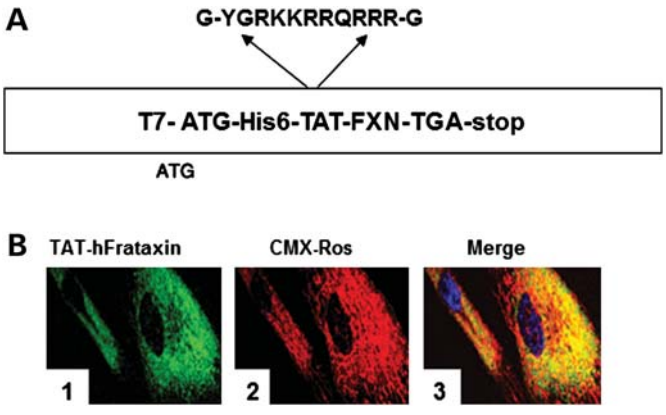

Figure 1. Expression and application of TAT-human frataxin (TAT–FXN). (**A**) Domains of TAT–FXN fusion protein. Expression is driven by the T7 promoter, and purification is based on a 6X-His tag. The TAT peptide sequence is expanded and placed at the N terminus of the human precursor FXN cDNA. (**B**) 5-IAF-labeled TAT–FXN incubated with FRDA human fibroblasts and imaged live by confocal microscopy. 5-IAF primarily reacts with sulfhydryl groups, but can also react with methionine, histidine and potentially tyrosine. Mitochondria are stained with CMX-rosamine. TAT–FXN is green (panel 1), mitochondria are red (panel 2) and signal co-localization is yellow (panel 3). Panels 1–3 are 120 h after a 3 h exposure to TAT–FXN.

to TAT–FXN, the cells were incubated with the mitochondrial-specific fluorescent dye, CMXRos (MitoTracker Red) (42,43), which localizes to mitochondria on the basis of the membrane potential, $\Delta\Psi m$, and imaged as live cells by confocal microscopy. Figure 1B shows the green fluorescein from labeled TAT–FXN (panel 1), the red signal from mitochondrial uptake of MitoTracker Red (panel 2) and co-localization of both signals from mitochondria in panel 3. Previous work had shown that the TAT moiety must be removed after transduction into mitochondria or else it moves out of the mitochondrial matrix within 2 h (35,38). The continued presence of TAT–FXN in the mitochondria 120 h after treatment suggests that the TAT–FXN was processed *in vivo* by the mitochondrial MPP to remove the FXN MTS with its attached TAT peptide, thus leaving the processed FXN in the matrix.

TAT–FXN is processed by the MPP

To demonstrate that the TAT–FXN fusion protein would be appropriately recognized and cleaved by the MPP, we expressed and purified yeast MPP (44) to demonstrate processing of the precursor FXN. The fusion protein, TAT-mitochondrial malate dehydrogenase-enhanced green fluorescent protein (TAT-mMDH-eGFP), was used as a positive control because it has been shown to transduce into mitochondria *in vivo* and processed, and TAT–GFP was a negative control (38).

Figure 2A shows that the control, TAT–mMDH–eGFP, is progressively processed to completion by an overnight incubation with MPP as predicted. The upper band (upper arrowhead) is the precursor protein of TAT–mMDH–eGFP as shown by the starting material in lane 0. A decrease in signal from the precursor band is seen with increasing incubation time (1, 3 h, overnight) with an increase in signal from the processed band (lower arrowhead). There are two cleavage

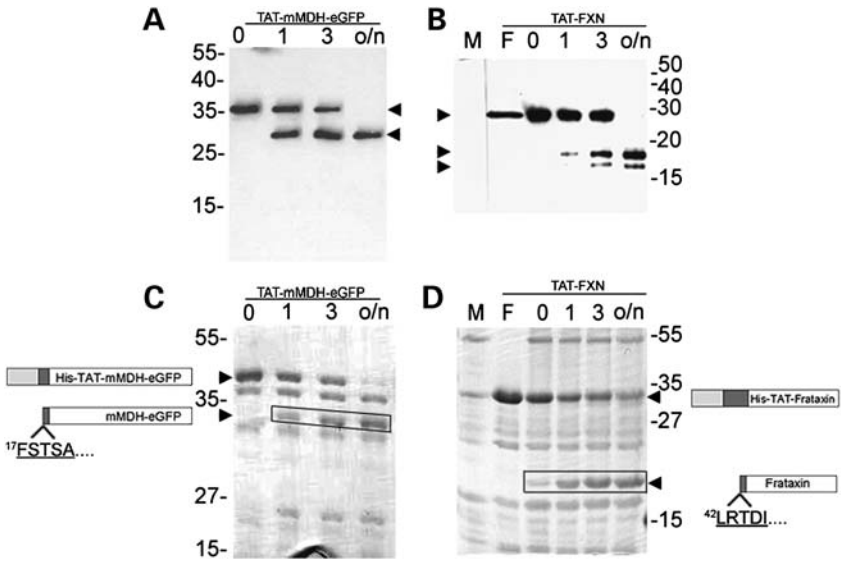

Figure 2. Processing of TAT–FXN by mitochondria processing peptidase (MPP). (**A**) Western blot showing progressive cleavage of TAT–mMDH–eGFP and probed with anti-GFP. Lanes 0 (starting condition), 1, 3 h and overnight (o/n) incubation with MPP at 37°C. Upper arrow is precursor band, and lower arrow is processed band. (**B**) Western blot of TAT–FXN cleavage by MPP and probed with anti-human FXN monoclonal antibody. Lanes as in (A). Upper arrow is precursor band and lower arrows show intermediate and mature processed FXN. Lanes include MPP (M), which was run on the same gel but is not contiguous, and precursor TAT–FXN (F) not exposed to MPP. (**C**) Reaction products of (A) were separated by 12% sodium dodecyl sulfate polyacrylamide gel electrophoresis (SDS–PAGE) and stained by Coomassie. Lanes are as marked in (A). Cartoon of precursor TAT–mMDH–eGFP is shown beside precursor band (upper arrow), and cartoon of processed band is shown next to lower arrow. Light grey is the His–TAT moiety, dark grey is the mMDH mitochondrial targeting sequence (MTS) and white is eGFP (drawn to scale). Boxed bands were sequenced by Edman degradation and the first 5 sequenced amino acids are shown as underlined single letter codes (Panels C and **D**). (D) Reaction products of (B) were separated by 12% SDS–PAGE, and boxed bands were sequenced. Upper cartoon shows precursor TAT–FXN (drawn to scale) with shaded regions as in (C) except that dark grey is the native FXN MTS. Cartoon of processed intermediate band is shown with the first 5 amino acids identified by Edman degradation. Numbers next to first amino acid in (C) and (D) refer to the position of the amino acid in the native mMDH and FXN precursor proteins, respectively.

sites within the MTS of the rat mMDH protein (45,46) with the first cleavage site generating an intermediate size protein from the loss of the TAT peptide and part of the MTS (an estimated protein mass of 3.2 kDa), and a second cleavage site to generate the mature mMDH by the loss of an additional 0.8 kDa protein mass. Figure 2C shows separation of these reaction products by sodium dodecyl sulfate polyacrylamide gel electrophoresis (SDS–PAGE) and staining by Coomassie. Sequencing of the lower molecular weight band (boxed area) by Edman degradation confirms processing of the TAT–mMDH–eGFP at the first protease sensitive site beginning at amino acid 17 of the precursor mMDH protein. This is in agreement with earlier published data of mMDH processing in mouse (26) and rat (45) for which the cleavage site exactly matches these results (FSTSA). That the TAT–mMDH–eGFP is not processed to maturity at the second predicted protease sensitive site supports earlier findings that this site is cleaved by the mitochondrial intermediate protease in the matrix, which is not present in these reactions (26,47).

Figure 2B and D shows that TAT–FXN is also appropriately recognized and processed by the MPP. Figure 2B is a western blot probed with a monoclonal anti-human FXN antibody showing the TAT–FXN precursor band (upper arrowhead), and Figure 2D is a Coomassie-stained SDS–PAGE of these reaction products. With progressive incubation times, there is an increase in the intermediate band (middle arrowhead in Fig. 2B, lower arrowhead in Fig. 2D), and a smaller band in Figure 2B (lower arrowhead). The TAT–FXN is processed to completion in an overnight digest (lane o/n).

The boxed area of the gel in Figure 2D was sequenced by Edman degradation and yielded the peptide fragment, LRTDI, shown in the cartoon at the lower arrowhead in Figure 2D. This peptide fragment corresponds exactly to the first cleavage site of human FXN at position 42 of the precursor FXN protein leading to the intermediate form (27). Unlike TAT–mMDH–eGFP, it appears that TAT–FXN is fully processed at the second cleavage site (position 81) to the expected size of the mature form by yeast MPP as shown by the predicted lower signal (lower arrowhead in Fig. 2B). This finding is consistent with earlier studies, showing that MPP alone is responsible for generating the intermediate and mature forms of FXN (27). However, this lower band was too faint to positively identify from the stained SDS–PAGE gel and could not be cut out for sequencing by Edman degradation. This is also consistent with earlier studies showing that conversion of the intermediate to mature forms of FXN is rate limiting *in vitro* (27).

In these experiments, TAT–GFP (no MTS) was used as a negative control and did not demonstrate any processing by the MPP on either a western blot using anti-GFP antibody, or by SDS–PAGE and staining as expected (see Supplementary Material, Fig. S2). This confirmed that the MPP was specific for the MTS in these mitochondrial fusion proteins and did not generate a non-specific protease action.

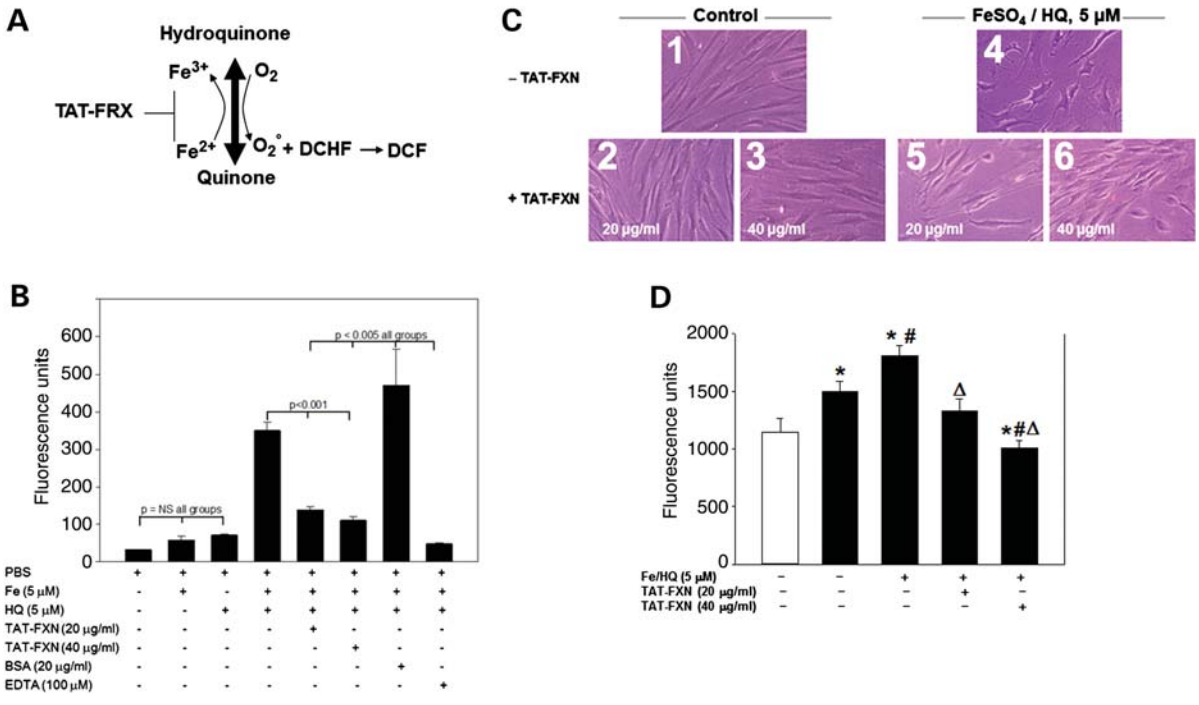

Figure 3. TAT–FXN binds iron and rescues FRDA cells from iron-oxidant stress. (**A**) Basis for an iron-binding assay for TAT–FXN. (**B**) TAT–FXN (20 or 40 μg/ml) was incubated in PBS in the presence of 5 μM each of ferrous sulfate (Fe) and HQ. Superoxide generation was measured by DCF fluorescence and expressed as arbitrary fluorescence units (*y*-axis). BSA (20 μg/ml) was used as a negative control and EDTA was used as a positive control. Data represents mean (± SD) of nine replicates of each condition. Significant statistics marked above columns. (**C**) FRDA fibroblasts (cell line GM04087, Coriell Institute) were grown to 80% confluence and treated with either 20 or 40 μg/ml of TAT–FXN, or with PBS vehicle (–TAT–FXN), after which the culture media was changed to control conditions (TAT–FXN removed from media). Cells were exposed to Fe/HQ for 5 h, or cultured in standard media (Control). (**D**) Fibroblasts from a healthy age- and sex-matched control (clear bar) (cell line GM01661, Coriell Institute) or from FRDA fibroblasts (black bars) were treated as in (C), washed with PBS and assayed for caspase-3 activation after normalizing for total protein loading. The data represents the mean (± SD) of three replicates of each condition analyzed by Student's *t*-test. * = $P < 0.001$ versus healthy control. $^{\#}P < 0.005$ vs FRDA and $^{\Delta}P < 0.001$ versus FRDA + Fe/HQ.

TAT–FXN binds iron in a cell-free system

FXN is predicted to have an iron-binding role that supports the formation of Fe–S clusters in proteins, such as aconitase, and in the biosynthesis of heme (48,49). The ability of TAT–FXN to bind iron was determined *in vitro* using the redox cycle of hydroquinone (HQ) to quinone (50) to generate a signal. As shown in Figure 3A, HQ can auto-oxidize to quinone thus generating the superoxide free radicals (51), which can be assayed by oxidation of the non-fluorescent reactive dye 2′,7′-dichlorodihydrofluorescence diacetate (DCHF-DA) to the fluorescent dye 2′,7′-dichlorofluorescein (DCF). The oxidized quinone is then reduced to HQ by ferrous sulfate, which is present in the incubation. We predicted that if TAT–FXN bound free iron, there would be a reduction of free iron content capable of reducing quinone back to HQ and a corresponding decrease in the production of superoxide. This could be quantified by a decrease in fluorescent signal from DCF.

Figure 3B shows that the precursor FXN molecule (as TAT–FXN) can bind iron *in vitro*. In phosphate buffered saline (PBS), DCHF has a basal amount of auto-fluorescence. When ferrous sulfate or HQ is added separately in PBS, there is no significant augmentation of the fluorescent signal. However, when ferrous sulfate and HQ are combined (as Fe/HQ), there is an active redox cycle thus generating superoxide and a significant signal compared with the previous conditions ($P < 0.001$). Additionally, the superoxide pool is depleted by the DCHF fluorescent dye, which drives the forward oxidation reaction of HQ to quinone at a higher rate. When TAT–FXN is introduced in the incubation, it binds free ferrous and ferric ions (52) resulting in a statistically significant reduction in the fluorescent signal with increasing amounts of TAT–FXN protein (Fig. 3B). Bovine serum albumin (BSA) was used as a negative protein control to determine the impact of non-specific binding of protein to free iron. Ethylenediaminetetraacetic acid, which is a metal chelator, was used as a positive control to demonstrate a reduction in reactive oxygen species formation, thus confirming the role of iron in the generation of superoxide under these conditions.

TAT–FXN can rescue FRDA fibroblasts from an iron-oxidant stress

In the absence of FXN, it is widely accepted that deficient cells will have an increased sensitivity to oxidative stress, which most likely contributes to the cascade of events leading to cytotoxicity (53–55). Iron with HQ induces an oxidative stress to cells (56–58) because HQ also forms a lipophilic chelate with iron and rapidly transfers the metal across the normally impermeable plasma membrane (59). Neither HQ nor Fe alone in culture media is toxic to FXN deficient

fibroblasts even after an extended exposure of 24 h (Supplementary Material, Figure S3). Thus, FXN-deficient cells were treated with TAT–FXN 24 h earlier followed by changing to media without TAT–FXN prior to treating with 5 μM Fe/HQ for 5 h (Fig. 3C). Treatment with TAT–FXN by itself had no effect on the cells (Fig. 3C, control panels 2 and 3) and they appear as untreated cells (panel 1). However, when these cells were treated with Fe/HQ, changes in the morphology (rounded and spiculated cells) and loss of adherence of these cells indicated that Fe/HQ was cytotoxic (Fig. 3C, panel 4). In contrast, cells that were treated with TAT–FXN prior to the addition of Fe/HQ (panels 5 and 6) were able to survive and had reduced evidence of cytotoxicity as shown by their morphologic appearance being identical to control cells (panel 1).

TAT–FXN reduces caspase-3 activation in FRDA fibroblasts exposed to iron-oxidant stress

To determine whether TAT–FXN is capable of protecting FRDA cells against apoptosis after exposure to Fe/HQ-oxidant stress, FXN-deficient patient fibroblasts, or fibroblasts from a control patient without FRDA, were assayed for caspase-3 activation under baseline conditions and again after exposure to an iron-oxidant stress.

In Figure 3D, caspase-3 activation was significantly elevated ($P < 0.001$) in fibroblasts from a patient with FRDA when compared with fibroblasts from a healthy control patient. After exposure to an iron-oxidant stress, the same FRDA fibroblasts expressed significantly greater amounts of activated caspase-3 compared with baseline FRDA fibroblasts ($P < 0.001$). Treatment of FRDA fibroblasts with TAT–FXN prior to the introduction of an iron-oxidant stress was significantly protective against activation of caspase-3 when compared with Fe/HQ-treated FRDA fibroblasts ($P < 0.001$). As expected, there was no significant difference in caspase-3 activation between the control fibroblasts and FRDA fibroblasts exposed to Fe/HQ and treated with TAT–FXN ($P > 0.05$). This protection was dose related and was not due to the presence of TAT–FXN in the culture media because the fusion protein had been removed 24 h prior to introduction of the iron-oxidant stress. At 40 μg/ml, the amount of caspase-3 activation was below the baseline of the FRDA fibroblasts ($P < 0.001$).

TAT–FXN increases the survival rate and lifespan in *Fxn*-KO mice

The ability of TAT–FXN to protect FXN-deficient patient fibroblasts against Fe/HQ stress *in vitro* provided a strong rationale for determining whether a TAT–FXN fusion protein could rescue the *Fxn* knock out (*Fxn*-KO) mouse. Because the homozygous deletion of the *Fxn* gene is embryonic lethal (60), mice conditional for deletion of exon 4 of the *Fxn* gene (33) were studied using the NSE-Cre transgene (61–63) to generate progeny with the loss of FXN in heart and neural crest-derived tissues. Two groups of mice were examined for rescue with a TAT–FXN fusion protein: *Fxn*-KO mice receiving either TAT–FXN protein or PBS beginning at Day 3 of life (designated as 3d) until study end at 60 days of life, and *Fxn*-KO mice receiving either TAT–FXN protein or no PBS beginning at Day 12 of life ± 2 days (designated as 12d) and continuing until death (end of life study). All mice had to reach an age of 10 days to be included in the study, and all mice were weaned at 28 days of age. Control animals consisted of littermates heterozygous for the conditional allele (L3/+) carrying or not carrying the recombinase, and had no clinical or biochemical phenotype (33). *Fxn*-KO mice in the 3d group received intraperitoneal (IP) injections three times per week, with either 15 mg/kg body weight of TAT–FXN, or an equivalent volume of sterile PBS. Dosing in the *Fxn*-KO 3d group was stopped at 60 days of life (end of study). The 3d control heterozygous littermates received equivalent volume injections of PBS. *Fxn*-KO mice in the 12d group received either TAT–FXN 20 mg/kg body weight (100 μl injections) given by the IP route beginning at 12 days of life ± 2 days twice weekly until death, or no injections of PBS. The 12d control heterozygous littermates did not receive injections.

The lengths of survival for both 3d and 12d groups were analyzed using the Kaplan–Meier estimator with log-rank sums to test the null hypothesis that there was no difference between populations in the probability of a death at any time point (64). The results are shown in Figure 4A and B. Pairwise multiple comparisons between all combinations of pairings (Holm–Sidak method) were performed to determine significance between groups and are shown in Table 1. By log-rank sums' treatment with TAT–FXN beginning either at 3 days of age (3d group), or 12 days of age (12d group), resulted in a highly significant increase in lifespan of the *FXN*-KO mouse. In the 3d group, treatment with TAT–FXN extended the mean survival of the *Fxn*-KO mouse by ~49% to 41.1 ± 4.3 days and was significant ($P = 0.008$) when compared with the mean age at death of 27.5 ± 2.3 days in the *Fxn-KO* mouse receiving only PBS (Table 1). It is noteworthy that five mice (31%) reached the end of the study at 60 days and died when TAT–FXN was discontinued, whereas no mouse in the PBS group reached this age and only one mouse survived beyond 35 days. In the 12d group, treatment with TAT–FXN extended the mean survival of the *Fxn-KO* mouse by ~53% to 43.1 ± 4.2 days and was significant ($P = 0.003$) when compared with the mean age at death of 28.1 ± 1.4 days in the *Fxn-KO* mouse not receiving PBS (Table 1). It is noteworthy that five mice (16%) exceeded 60 days of life with two mice expiring at 75 and 88 days. No mouse in the untreated group exceeded 40 days of life. There was no significant difference in the mean age at death between the 3d and 12d *Fxn-KO* mice receiving TAT–FXN, and in agreement with the original characterization of the model (33), there was no significant difference in the mean ages of death between the *Fxn-KO* mice receiving PBS (3d) versus no PBS (12d). In the 12d KO no PBS group, 6 of 29 animals (21%) were removed (censored) prior to the end point of death for biochemical and histological studies, whereas 8 of 32 (25%) in the 12d KO TAT–FXN group were censored for the same reasons and are accounted for in the Kaplan–Meier analysis.

The survival rate of animals was examined by determining the number of animals surviving 10% longer beyond the mean age of death of the untreated 12d *Fxn-KO* mouse of 28.1 ± 1.4

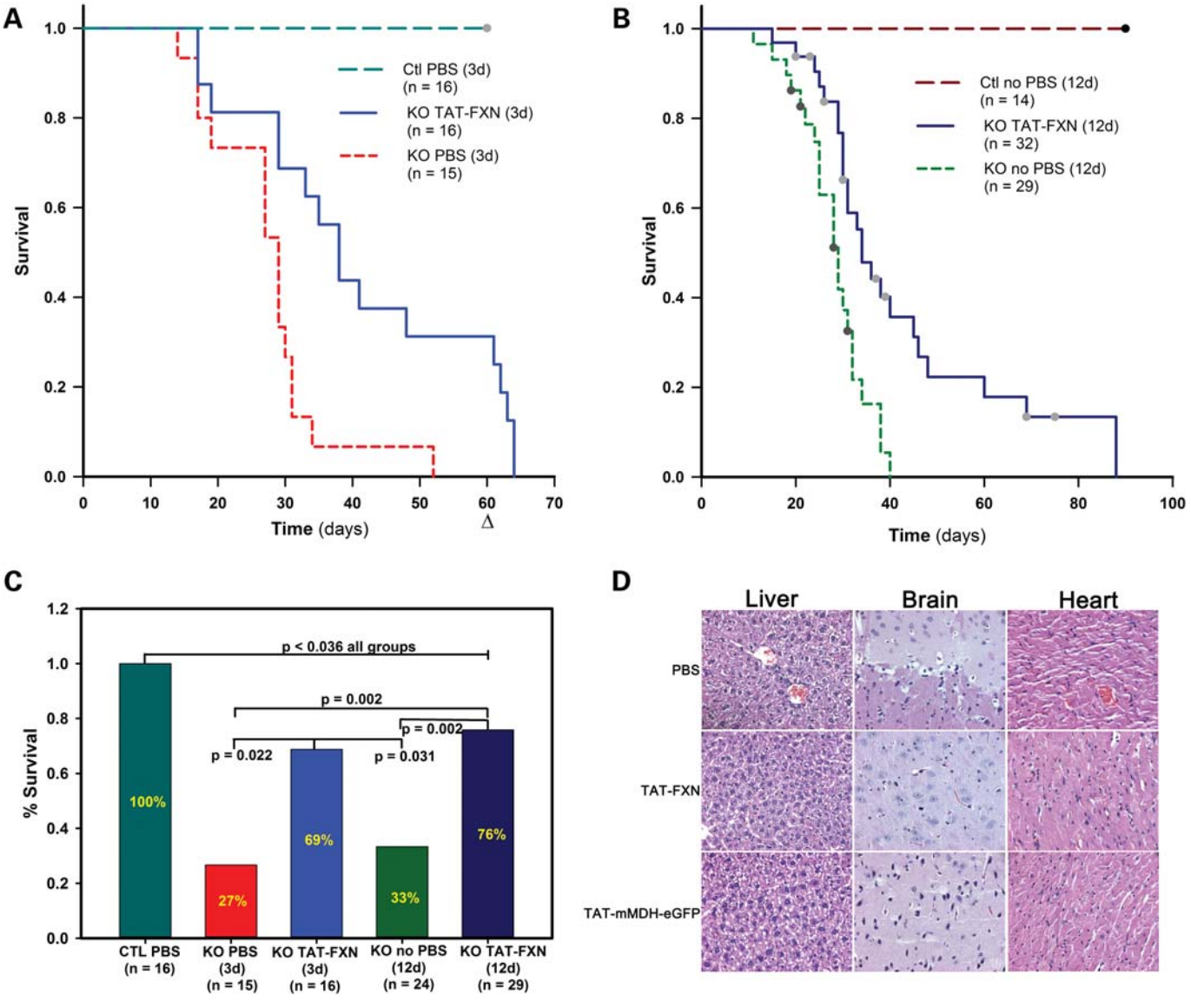

Figure 4. Survival analysis. (**A**) Treatment begun at 3 days of age. Groups: KO PBS (3d) = *Fxn-KO* mouse with PBS beginning at 3d of age. KO TAT–FXN (3d) = *Fxn-KO* mouse with TAT–FXN beginning at 3d of age. Ctl PBS = heterozygous age-matched littermates with PBS injections beginning at 3d. Study terminated at 60 days (=Δ). (**B**) Treatment begun at 12 days of age. Groups are as follows: KO no PBS (12d) = *Fxn-KO* mouse without PBS treatment starting at 12d; KO TAT–FXN (12d) = *Fxn-KO* mouse with TAT–FXN treatment starting at 12d; Ctl no PBS = heterozygous age-matched littermates without PBS injections. Filled circles represent censored event. Study continued to end of life. (**C**) Survival of groups to 31 days of age and beyond with significance ($P \leq 0.05$) for relevant groups using Student's *t*-test. The 12d groups are adjusted for censoring prior to 31 days, which lowers their total numbers when compared with (B). (**D**) Two-month-old heterozygous female mice were injected with PBS (100 μl/injection), TAT–FXN or TAT-mMDH-eGFP, each at 2 mg/kg/week (total protein) for 2 months per IP route. Tissues were fixed in 10% formalin and stained by hematoxylin and eosin.

days. Figure 4C shows that the TAT–FXN-treated animals in both the 3d and 12d groups had significantly higher survival rates to 31 days of age and beyond. Of the 3d group, 69% of the TAT–FXN group survived to 31 days and beyond compared with only 27% of the PBS-treated group ($P = 0.022$). Of the 12d group, 76% of the TAT–FXN-treated animals survived to 31 days and beyond compared with 33% of the untreated *Fxn-KO* animals ($P = 0.002$). The 12d groups were adjusted for censoring prior to 31 days of age. There was no significant difference in survival rates between the 3d and 12d KO TAT–FXN animals, nor between the survival rates of the 3d *Fxn-KO* PBS and 12d *Fxn-KO* no PBS mice. The control heterozygous mice with PBS injections predictably had no deaths and were significantly different from all *Fxn-KO* mice groups.

Finally, histology of organs was performed as a control to evaluate possible tissue inflammatory response to chronic IP injections of TAT-fusion proteins. Two different TAT-fusion proteins, TAT–FXN and TAT-mMDH-eGFP (38), and the PBS carrier fluid were injected into adult 2-month heterozygous control female mice twice weekly for 2 months. There was no evidence of inflammation in the liver, brain or heart as shown by the lack of inflammatory cells (Fig. 4D).

Table 1. Survival significance

Group	Death (d) (± SEM)	KO + TAT–FXN (3d)	KO + PBS (3d)	CTL + PBS (3d)	KO + TAT–FXN (12d)	KO no PBS (12d)	CTL no PBS (12d)
KO + TAT–FXN (3d)	41.1 ± 4.3d	–	0.008*	<0.001	NS	0.007*	<0.001
KO + PBS (3d)	27.5 ± 2.3d	0.007*	–	<0.001	0.007*	NS	<0.001
CTL + PBS (3d)	60 ± 0d	<0.001	<0.001	–	<0.001	<0.001	NS
KO + TAT–FXN (12d)	43.1 ± 4.2d	NS	0.007*	<0.001	–	0.003*	<0.001
KO no PBS (12d)	28.1 ± 1.4d	0.007*	NS	<0.001	0.003*	–	<0.001
CTL no PBS (12d)	90 ± 0d	<0.001	<0.001	NS	<0.001	<0.001	–

Survival curves of groups were analyzed with pairwise multiple comparison procedures (Holm–Sidak method) using an overall significance of $P = 0.05$.

TAT–FXN increases the growth velocity of the Fxn-KO mice

Growth velocity as a percentage of body weight was calculated for the three groups (12d) using the two-point average weight model (reviewed in 65) across the time period of 7–10 days after injections with TAT–FXN were started in the treated group. We tested the null hypothesis that the growth between treated and untreated *Fxn-KO* mice would be the same. Growth velocity is most commonly expressed as g/kg body weight/day, but was modified for mice to reflect their smaller weight and is expressed as g/g starting weight/day × 100%.

The results were analyzed by ANOVA for significance with Dunn's method for pairwise multiple comparisons (Fig. 5). The control littermate animals experienced a mean growth velocity of 4.67 ± 1.97% per day. The median for this group was 4.38% with a range of 3.39% (25%) to 5.96% (75%). By comparison, the KO TAT–FXN (12d) animals grew significantly slower than controls with a mean growth velocity of 1.97 ± 3.36% per day ($P < 0.05$). The median of this group was 1.55% with a range of 0.21% (25%) to 4.178% (75%). Notably, however, the growth velocity of the KO TAT–FXN (12d) animals was significantly higher than the KO no PBS (12d) ($P < 0.05$) animals. In agreement with the previous characterization of the model (33), the KO no PBS (12d) animals had negative growth velocities across this time frame with a mean of −1.04 ± 1.92%, indicating that they were losing weight rather than gaining as seen in the other two groups. The median growth velocity of the KO no PBS (12d) group was −0.465% with a range of −2.368% (25%) to 0.455% (75%). Finally, the growth velocity of the KO no PBS (12d) was significantly lower than that of the control group ($P < 0.05$).

Table 2 shows the characteristics of these three groups. There were no differences in the starting or ending ages during which these measurements were made, indicating that the animals were at equivalent periods of growth in their lives. As expected, the starting weight of the control animals was significantly higher ($P < 0.05$) than either of the KO TAT–FXN (12d) or of the KO no PBS (12d) animals, but there was no significant difference between the starting weights of the two groups of *Fxn-KO* animals. All of the control animals gained weight (% positive weight gain) and 79% of the KO TAT–FXN (12d) animals gained weight (P = NS). However, only 30% of the KO no PBS (12d) animals showed any weight gain across this period, which was significantly lower ($P < 0.05$) than either the KO TAT–FXN (12d) group (indicated by the '#') or the control group (indicated by the '*'). At the end of the study, the control group animals had a mean weight of 11.3 ± 1.78 g, which was significantly higher than either KO TAT–FXN (12d) (6.8 ± 1.90 g) or KO no PBS (12d) (5.7 ± 1.68 g) animals ($P < 0.001$ for both). The KO no PBS (12d) animals were significantly smaller than the KO TAT–FXN (12d) animals at the end of the measurement period ($P < 0.016$).

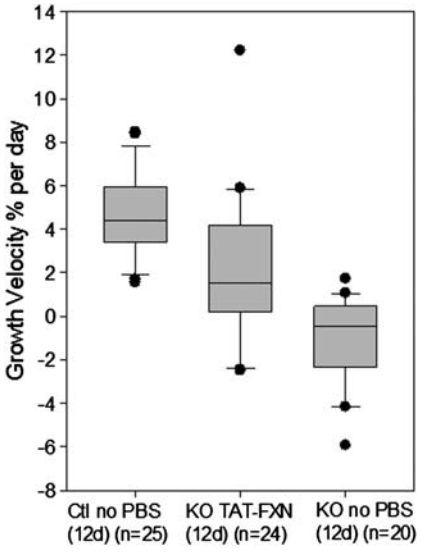

Figure 5. Growth velocity was calculated for the three groups as follows: [(EndWt − StartWt)/StartWt] × [100% /(EndAge − StartAge)]. The growth velocity for each animal was calculated and averaged for each group, and then plotted as median, 75 and 25% (upper and lower box limits). Groups are as follows: Ctl no PBS = heterozygous age-matched littermates without PBS injections. KO TAT–FXN (12d) = *FXN-KO* mouse with TAT–FXN treatment starting at 12d; KO no PBS (12d) = *FXN-KO* mouse without PBS treatment starting at 12d.

TAT–FXN increases the activity of aconitase in the heart of the *Fxn*-KO mouse

Aconitase is a mitochondrial enzyme with Fe–S clusters. The loss of FXN has been shown to decrease its activity in both cell culture models (66), and *in vivo* (33,67). We tested the hypothesis that *Fxn-KO* animals treated with TAT–FXN would

Table 2. Growth characteristics of mice

Group	*n*	Start Wt	End Wt	Start Age	End Age	% Positive Wt gain
Controls	25	8.20 ± 1.88 g	11.30 ± 1.78 g	13.1 ± 3.1d	21.6 ± 2.5d	25/25 (100%)
Treated	24	5.92 ± 1.64 g[a]	6.84 ± 1.90 g[a]	12.7 ± 3.3d	21.4 ± 2.9d	19/24 (79%)
Untreated	20	6.11 ± 1.49 g[a]	5.71 ± 1.68 g[a,b]	14.3 ± 2.7d	23.2 ± 2.9d	6/20[a,b] (30%)

Values are the group means ± standard deviation.
[a]Significantly different from the control group ($P < 0.05$).
[b]Significantly different from the treated group ($P < 0.05$).

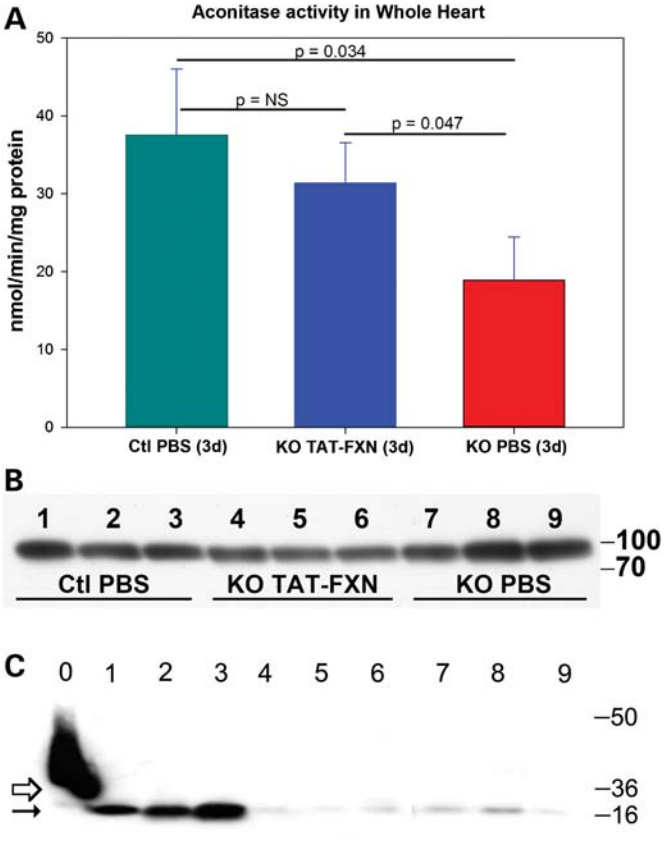

Figure 6. (**A**) Aconitase-specific activity in heart. Ctl PBS (3d) = heterozygous littermates receiving PBS from 3 days of life. KO TAT–FXN = *FXN-KO* (3d) mice treated with TAT–FXN beginning at 3 days of age. KO PBS = *FXN-KO* (3d) mice treated with PBS beginning at 3 days of age. Aconitase-specific activity on *y*-axis. $N = 3$ per group with triplicate assays, and analyzed by Student's *t*-test. (**B**) Western blot of mitochondrial aconitase protein from the mouse hearts in 'C' containing 25 μg of total protein per lane. Lanes 1–3 = Ctl, lanes 4–6 = KO TAT–FXN, lanes 7–9 = KO PBS. The lanes were scanned and signal quantified using MetaMorph software (reported in text). M_r in kDa for (B) and (C). (**C**) Recovery of processed TAT–FXN from heart (small arrow). Lane 0 = injected TAT–FXN (large arrow). Lanes 1–3 are *FXN-KO* animals receiving TAT–FXN (12d). Lanes 4–6 are *FXN-KO* no PBS (12d) animals. Lanes 7–9 are heterozygous littermates [Ctl no PBS (12d)] and were run on the same gel but are not contiguous.

have a higher activity of aconitase in their hearts when compared with untreated KO animals.

Using three age-matched animals in each group: heterozygous littermates given PBS as controls (Ctl), KO TAT–FXN (3d) and KO + PBS (3d), total aconitase activity was determined from heart homogenates by monitoring the formation of NADPH by isocitric dehydrogenase following the aconitase-dependent conversion of citrate to isocitrate (Cayman Chemical). In Figure 6A, the specific activity of aconitase from each group of animals shows that TAT–FXN is able to reconstitute activity of aconitase in the KO TAT–FXN group. The specific activity of aconitase from the heterozygous littermate control group, Ctl PBS (3d), was 37.52 ± 8.54 nmol/min/mg protein, and that of the KO TAT–FXN (3d) group was 31.36 ± 5.19 nmol/min/mg protein (P = NS). In contrast, the KO PBS (3d) group was significantly lower than both the Ctl and KO TAT–FXN (3d) groups at 18.91 ± 5.55 nmol/min/mg protein.

Western blotting was performed where the same samples were assayed for mitochondrial aconitase (Fig. 6B). This shows that mitochondrial aconitase protein mass is increased in the samples from the KO PBS (3d) group when compared with the Ctl and KO TAT–FXN groups. Densitometry of the Ctl PBS group averaged 7428 ± 358 pixels, the KO TAT–FXN group averaged 6787 ± 259 pixels, and the KO PBS group was 9068 ± 1292 pixels. There was significantly greater mitochondrial aconitase protein mass in the KO PBS group than in the KO TAT–FXN group ($P = 0.04$), and there was no significant difference between the Ctl PBS and KO TAT–FXN groups. Taking Figure 6A and B together, mitochondrial aconitase protein mass is increased in the KO PBS mice while total aconitase activity is decreased. In contrast, in the KO TAT–FXN group, aconitase activity and protein mass are restored to near Ctl levels. These data are consistent with recent findings showing that mitochondrial assembly of Fe–S clusters is necessary for cytosolic Fe–S-dependent proteins (68–70), as well as mitochondrial Fe–S-dependent enzymes.

To show that human FXN was present and processed in the hearts from the TAT–FXN-treated *Fxn-KO* mouse (Fig. 6C), western blotting was performed using whole heart homogenates from KO TAT–FXN (12d) mice ($n = 3$, lanes 1–3), KO no PBS (12d) mice with no injections ($n = 3$, lanes 4–6), and Ctl no PBS (12d) littermates ($n = 3$, lanes 7–9) with no injections. After separation on 12% SDS–PAGE and blotting, the membranes were probed using monoclonal antibody to human FXN (MitoSciences), which recognizes mouse FXN poorly. Lane 0 was loaded with the purified, precursor TAT–FXN that was injected and serves as a positive control. The *Fxn-KO* mice injected with TAT–FXN (lanes 1–3) demonstrate a strong signal at the estimated M_r of processed FXN of ~15 kDa. In contrast, there is essentially no signal in the *Fxn-KO* animals who did not receive

Table 3. Cardiac function in controls, treated KO and untreated KO mice

Group	Age, days	EF, %	FS, %	SV, μl	CO, ml/min	LVIDs, mm	LVIDd, mm	LVPWs, mm	LVPWd, mm	Ao peak, mm/s	E–A ratio
Ctl no PBS ± STDEV ($n = 12$)	33 ± 13.7	69.36 ± 8.65	38.62 ± 6.87	30.81 ± 7.47	10.96 ± 3.58	2.03 ± 0.35	3.30 ± 0.35	0.97 ± 0.18	0.58 ± 0.12	875.84 ± 172.75	2.079 ± 0.511
KO TAT–FXN ± STDEV ($n = 7$)	33.2 ± 12.6	38.69 ± 14.47[a]	18.50 ± 7.91[a]	14.64 ± 3.30[a]	5.06 ± 1.17[a]	2.59 ± 0.49[a]	3.16 ± 0.32	0.75 ± 0.14[a]	0.62 ±0.12	536.95 ± 114.11[a]	2.650 ± 1.075
KO no PBS ± STDEV ($n = 12$)	26 ± 4.1	40.99 ± 17.75[a]	20.70 ± 9.56[a]	14.15 ± 6.51[a]	3.19 ± 1.69[a,b]	2.47 ± 0.69[a]	3.06 ± 0.57	0.78 ± 0.18[a]	0.59 ±0.17	374.11 ± 169.46[a]	1.109 ± 0.862[a,b]

Number in each group is in parenthesis, and values are the group means ± standard deviation. Mitral valve inflow 'E'-wave to 'A'-wave ratio (E–A ratio) were measured.
EF, ejection fraction; FS, fractional shortening; SV, stroke volume; CO, cardiac output; LVIDs left ventricular internal diameter in systole; LVIDs left ventricular internal diameter in diastole; LVPW, LV posterior wall; Ao peak; aortic peak velocity.
[a]Significantly different from the control group ($P < 0.05$)
[b]Significantly different from the treated group ($P < 0.05$).

TAT–FXN (lanes 4–6) and only a faint signal of mature native FXN in the Ctl lanes (7–9). These data show that TAT–FXN is able to transduce into cardiac tissue to regenerate activity of Fe–S cluster-dependent enzymes.

TAT–FXN increases cardiac function in the *Fxn*-KO mouse

The increased aconitase activity in hearts of the *Fxn-KO* animals receiving TAT–FXN suggested that improved cardiac function might be responsible for their increased lifespan, survival rates and growth velocity compared with the untreated *Fxn-KO* animals. To test this hypothesis, cardiac function was non-invasively quantified in three groups of animals, Ctl no PBS (12d), KO TAT–FXN (12d), and KO no PBS (12d), using echocardiography as described in the Materials and Methods section. Mice were matched for their age at echocardiogram and there were no significant difference in ages between the 3 groups ($P = 0.192$, Table 3).

Figure 7A is a representative echocardiogram for each of the three groups. The M-mode column shows that the left ventricular contractile function and the heart rate are excellent in the control animal. Additionally, the KO TAT–FXN (12d) animal has visibly better left ventricular contractile function that is intermediate between the faster control animal and the KO no PBS (12d) animal indicating better systolic function.

Indices of cardiac function derived from the M-mode are shown in Table 3. As expected, all measures of systolic function, such as ejection fraction (EF), fractional shortening (FS) and stroke volume (SV) were significantly better in the control animals ($P < 0.05$). However, there were no significant differences in these indices between the KO TAT–FXN and KO no PBS animals. Consistent with the findings of decreased EF and FS in the *Fxn-KO* animals, the left ventricular internal diameter during systole (LVIDs) was significantly higher in treated ($P < 0.05$) and untreated *Fxn-KO* animals ($P < 0.035$) versus the controls indicating impaired systolic function in the KO animals. Surprisingly, the mean LVID during diastole (LVIDd) was not different between the three groups. The left ventricular posterior wall thickness during systole (LVPWs) was greater in controls consistent with their greater contractile function, and there was no significant difference in the LVPW thickness during diastole (LVPWd) between the three groups (~0.60 mm).

The velocity of blood flow in the ascending aorta is shown in the aortic Doppler column of Figure 7A. Aortic flow in the control animal is ~850 and ~700 mm/s in the KO TAT–FXN animal. In contrast, the untreated *Fxn-KO* animal has a lower velocity of blood flow, ~220 mm/s, consistent with the decreased left ventricular systolic function. This particular untreated animal (KO no PBS) also demonstrated the finding of pulsus alternans, which is a rhythmic attenuation of the pulse pressure frequently associated with heart failure (71). These findings for the three groups were quantified in Table 3. The aortic peak velocity is significantly higher in controls when compared with the two *Fxn-KO* groups, and the velocity trended toward significance in the KO TAT–FXN animals versus the KO no PBS animals but did not reach statistical significance ($P = 0.07$).

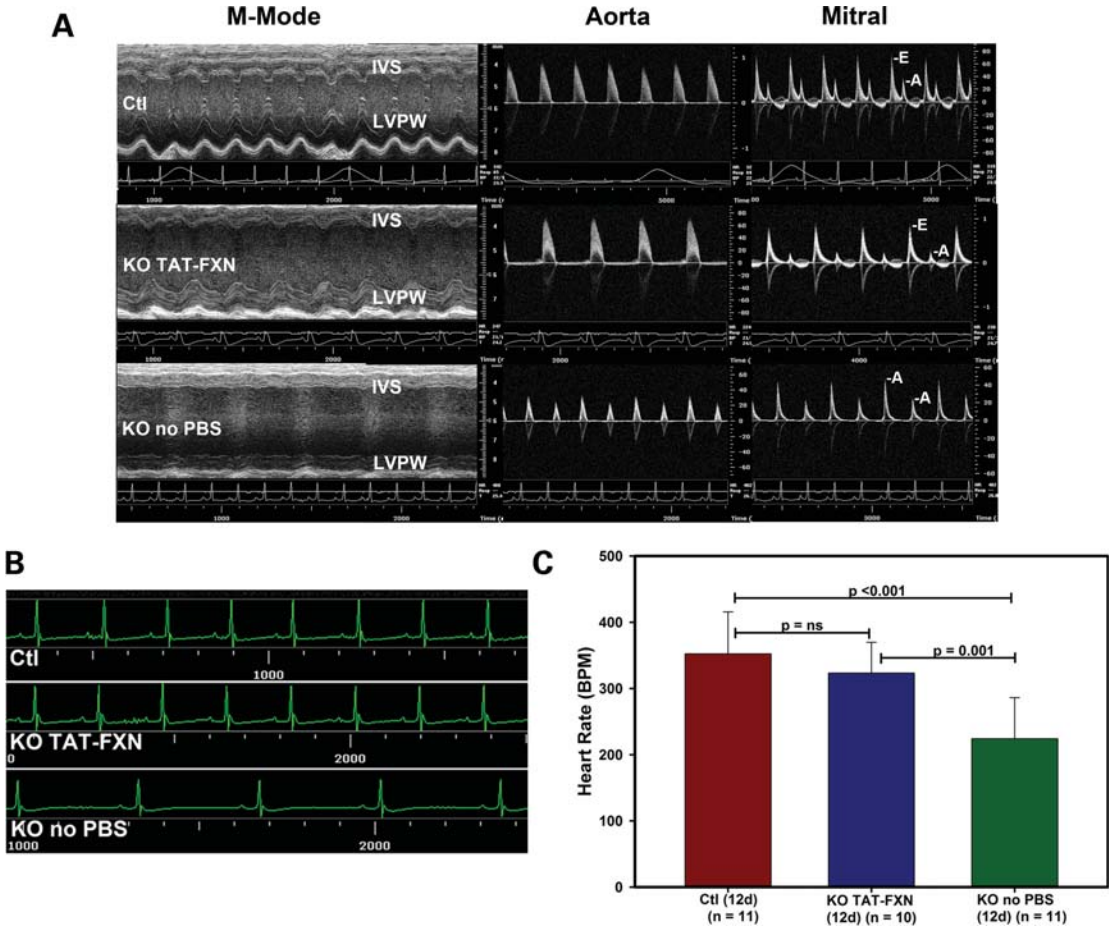

Figure 7. Echocardiography of FRDA animals. (**A**) Ctl = heterozygous littermates, no PBS (12d). KO TAT–FXN = *FXN-KO*-treated with TAT–FXN (12d). KO no PBS = *FXN-KO* without PBS (12d). The M-mode column shows the internal dimension of the left ventricle between the interventricular septum (IVS) and left ventricular posterior walls (LVPW). Scale in millimeters is on the right, and EKG is on the bottom. The aorta column shows the Doppler velocity of blood flow in the ascending aorta for all three groups. Note that the velocity scale for the Ctl animal is 1 m/s, whereas it is cm/s for the other two groups. The mitral column shows the Doppler mitral inflow pattern and velocity for all three groups. E-wave and A-wave are marked. The velocity scale on the right is cm/s for the Ctl and KO no PBS animals, and 1 m/s for the KO TAT–FXN animal. (**B**) The EKG from a representative animal in each of the three groups is shown. The heart rate was determined from the EKG of each mouse at the same time point during echocardiography. Note that the time scale (bottom) is in milliseconds. (**C**) The mean heart rate of all three groups analyzed by one-way ANOVA with pairwise multiple comparison procedures (Holm–Sidak method).

Finally, the mitral Doppler column (Fig. 7A) shows the velocity of blood flow into the left ventricle during diastole from the left atrium across the mitral valve. A normal transmitral flow pattern and velocity was present in the control animal where the ratio of the height of the E-wave to the A-wave (E–A ratio) was >1.5, which is associated with normal inflow into the left ventricle. A similar mitral inflow pattern was seen in the KO TAT–FXN animal. In contrast, the mitral inflow pattern in the KO no PBS animal showed absent E-waves with only A-waves remaining indicating impaired diastolic function of the left ventricle.

The E–A ratios were measured for 6 control animals (2.1 ± 0.51), 5 KO TAT–FXN animals (2.6 ± 1.07) and 11 KO no PBS animals (1.1 ± 0.86), and compared using ANOVA (Table 3). Notably, the E–A ratio was significantly higher in the KO TAT–FXN animals when compared with the KO no PBS animals ($P = 0.003$), higher in the control animals when compared with the KO no PBS animals ($P = 0.039$), and there was no significant difference between the controls and KO TAT–FXN animals ($P = 0.275$). The E–A ratio was >1.5 in all of the control animals (100%), 80% of the KO TAT–FXN animals and only 36% of the KO no PBS animals. The lower E–A ratios in the KO no PBS animals strongly suggest left ventricular diastolic dysfunction and a greater reliance on atrial systole to fill the left ventricle (72). These findings of decreased transmitral inflow and aortic Doppler velocities are similar to patients with FRDA in which myocardial velocity gradients during both systole and early diastole have been shown to be reduced (73).

The heart rates of the KO TAT–FXN animals were also significantly higher than the KO no PBS animals. A representative electrocardiogram (EKG) from Ctl no PBS (12d), KO TAT–FXN (12d) and KO no PBS (12d) animals is shown in Figure 7B, and quantitative data are shown in Figure 7C. The heart rates of the control and KO TAT–FXN animals were both 329 bpm, whereas the KO no PBS animals was 197 bpm. Figure 7C shows that the mean heart rates between controls

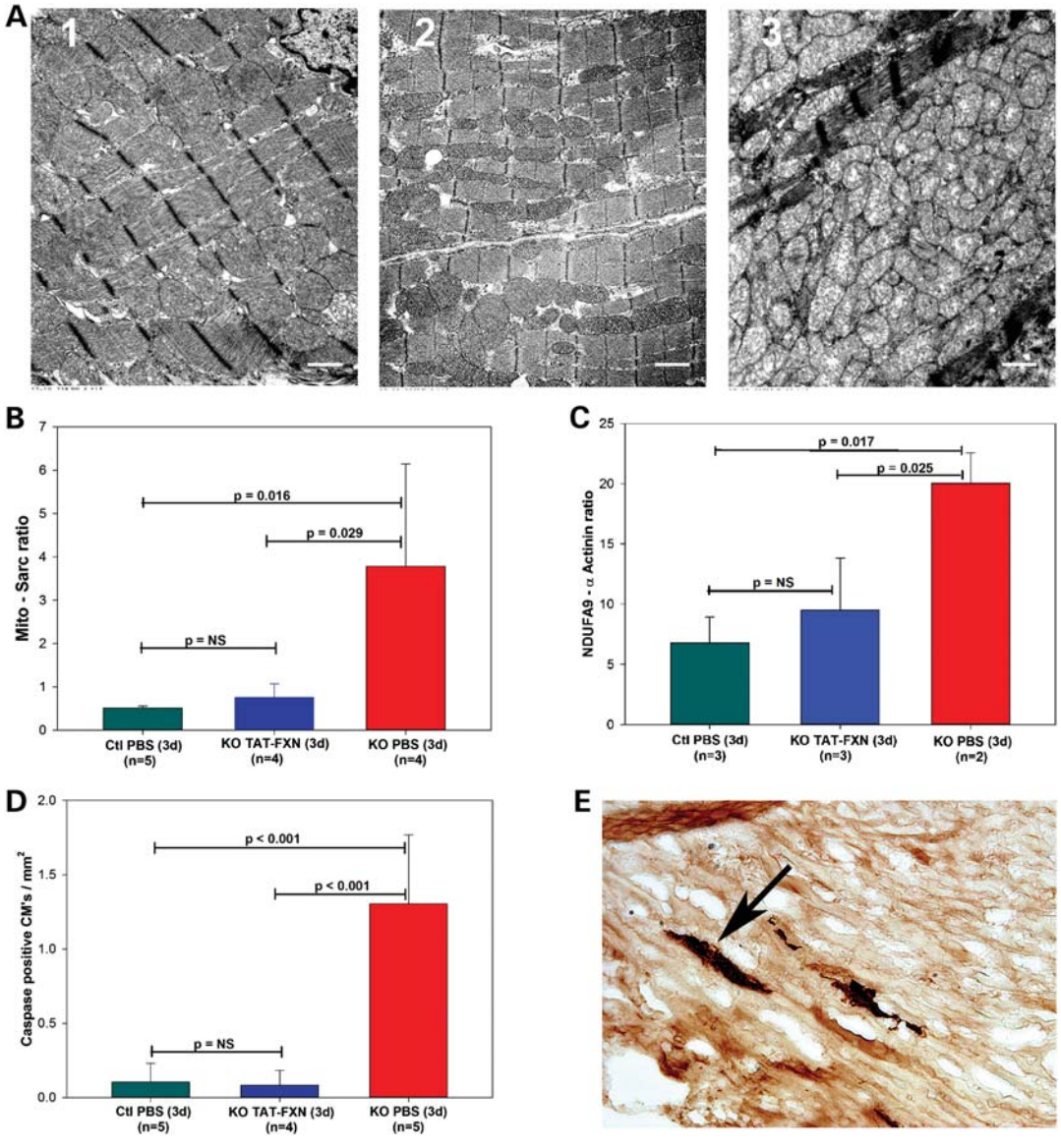

Figure 8. (**A**) EM of heart. Bar = 1 μm in all panels. 1 = Ctl PBS (3d). 2 = KO TAT–FXN (3d). 3 = KO PBS (3d). (**B**) Ratio of planimetry of mitochondria (Mito) to sarcomere (Sarc) area was determined using Photoshop to calculate area from EM. (**C**) Ratio of mitochondrial complex I protein (NDUFA9) to sarcomere α-actinin protein. All mice in (A)–(C) received injections beginning at 3 days of age (3d group) and all mice were assayed at 28 days of age. (**D**) Apoptosis counts of cardiomyocytes (CMs) in the heart from Ctl PBS (3d) at 28 days, KO TAT–FXN (3d) and KO PBS (3d) both at 26 ± 2 days. (**E**) Micrograph of caspase-3 activation in a 28d KO PBS (3d) heart. Arrow points to caspase-3-positive cardiomyocyte.

(358 ± 65) and KO TAT–FXN (349 ± 41) animals were not significantly different, but the KO no PBS mice (226 ± 59) were significantly lower than KO TAT–FXN or control mice ($P < 0.001$ for both comparisons). Although the measures of systolic function, such as EF, FS and SV, were not significantly different between KO TAT–FXN and KO no PBS animals, the higher heart rate and improved diastolic filling of the KO TAT–FXN animals translated into a significantly higher cardiac output (CO) when compared with the KO no PBS animals ($P = 0.02$).

In summary, these data show that the *Fxn-KO* animals treated with TAT–FXN had a higher CO due to a higher heart rate than the KO no PBS animals. Additionally, the KO TAT–FXN animals had significantly better diastolic function (higher E–A ratios) than the KO no PBS animals although their systolic function was not significantly different.

TAT–FXN maintains cardiac ultrastructure and reduces cardiomyocyte apoptosis in the *Fxn*-KO mice

Previous data had shown that cardiomyocyte ultrastructure was severely disturbed in the *Fxn-KO* mouse heart (33). In particular, there was marked proliferation of mitochondria, loss of myofibrils and disruption of the normal mitochondria–sarcomere relationship. We tested the hypothesis that hearts from animals treated with TAT–FXN would have normal ultrastructure as measured by mitochondrial number and appearance using electron microscopy (EM), and normal

myofibril content and relation to mitochondria. Three groups of mice, Ctl PBS (3d), KO TAT–FXN (3d) and KO PBS (3d), were studied at 28 days of age and the results are shown in Figure 8.

In panels A.1–3 are electron micrographs from three representative animals which include controls (A.1), TAT–FXN-treated *Fxn-KO* mice (A.2) and PBS-treated *Fxn-KO* mice (A.3). The control animal demonstrates normal mitochondrial morphology and numbers. The relationship of mitochondria to myofibrils is well ordered with virtually all mitochondria touching a myofibril and roughly one mitochondrion per sarcomere (74). In panel A.2, the TAT–FXN-treated *Fxn-KO* mouse heart shows essentially the same morphology as a normal control. Mitochondria are evenly distributed among the myofibrils and most of them measure one sarcomere in length. The number of sarcomeres per field is approximately the same as the controls. In contrast, the heart from a PBS-treated *Fxn-KO* mouse (A.3) shows markedly disrupted myofibril structure with very few sarcomeres per field, extensive dysmorphic mitochondrial proliferation and a loss of mitochondria to myofibril relationship. The mitochondria have widely varying sizes.

To quantify the results of EM imaging, planimetry of mitochondria and myofibrils was performed to calculate their respective cumulative areas on EM micrographs from multiple hearts (74,75). The results are expressed as a mitochondria-to-sarcomere ratio in Figure 8B. Both the controls ($n = 5$) and TAT–FXN-treated *Fxn-KO* mouse hearts ($n = 4$) have low ratios (<1) that are not statistically different from each other. In contrast, the PBS-treated *Fxn-KO* hearts ($n = 4$) have a much higher ratio (>3) of mitochondria to sarcomeres that is statistically significant when compared with both the controls and TAT–FXN-treated mice. This was confirmed by performing western blotting of heart tissue from all three groups to compare expression of a mitochondrial Complex I protein, NDUFA9, with expression of a contractile protein in heart, α-actinin. The results are shown in Figure 8C, and demonstrate that there is no significant difference in the ratio of mitochondria to sarcomeric protein mass in the control and KO TAT–FXN (3d) mouse heart. In contrast, the KO PBS (3d) mouse had significantly higher mitochondria to sarcomeric protein ratio when compared with the control or KO TAT–FXN (3d) mice.

To evaluate the heart for programmed cell death in the *Fxn-KO* mouse, hearts from Ctl PBS (3d) ($n = 5$), KO TAT–FXN (3d) ($n = 4$) and KO PBS (3d) ($n = 4$) were matched for age (26 days of life ± 2 days) and stained for caspase-3 activation as a marker of apoptosis. Cardiomyocytes positive for activated caspase-3 were identified based on rod-shaped morphology and staining, and quantified as described previously (76) (Fig. 8E). For each heart, five transverse sections across the left ventricle were counted completely and are plotted in Figure 8D. As expected, control mice had very low numbers of caspase-3-positive cardiomyocytes ($1.05 \times 10^{-5}/\mu m^2 \pm 1.26 \times 10^{-5}$). In contrast, the KO PBS (3d) mouse hearts had significantly higher numbers of caspase-3-positive cardiomyocytes ($1.37 \times 10^{-4}/\mu m^2 \pm 5.11 \times 10^{-5}$) when compared with control hearts ($P < 0.001$). Strikingly, the KO TAT–FXN (3d) hearts were not different from the controls ($8.48 \times 10^{-6}/\mu m^2 \pm 9.9 \times 10^{-6}$, $P = \text{NS}$), and were significantly less than the untreated KO PBS (3) hearts ($P < 0.001$).

Thus, the mitochondrial relationship to myofibrils is severely disrupted in the untreated *Fxn-KO* mouse heart, but is normalized by treatment with TAT–FXN. In concert with this finding, programmed cell death in the *Fxn-KO* mice treated with TAT–FXN is indistinguishable from the control hearts, and both are significantly lower than untreated *Fxn-KO* mouse hearts. These findings strongly support the conclusion that TAT–FXN fusion protein has rescued the cardiac function resulting in an increased lifespan and survival rate in the treated *Fxn-KO* mice.

DISCUSSION

The key finding from these experiments is that a cell-penetrant peptide is capable of delivering a replacement protein to mitochondria *in vivo* in amounts sufficient to rescue a very severe (fatal) disease phenotype. This has not been accomplished before and, in conjunction with other studies showing TAT-fusion proteins can restore mitochondrial enzyme activity in heterozygous mice (40), strongly supports the use of cell-penetrant peptides as a platform for developing novel therapeutic interventions for mitochondrial diseases. Mice homozygous for a conditional deletion of the *FXN* gene lived substantially longer and had an increased rate of survival when treated with TAT–FXN when compared with the untreated *Fxn-KO* group. Mature processed human FXN was recovered from *Fxn-KO* animals injected with TAT–FXN, indicating that the TAT–FXN reached the mitochondrial matrix. Analysis of cardiac function in these mice revealed that the treated animals had better diastolic function and a higher heart rate, which resulted in a higher CO even though both had evidence of impaired systolic function. This is important because diastolic dysfunction is a component of the heart disease of FRDA patients (73,77–79) and improvements in this parameter would be expected to improve heart failure and survival. The growth velocity was also improved in the treated animals. This was true even when dosing began later in life, i.e. 12 days of age, which has analogy to the typical age at diagnosis in humans (10). Histologic analysis of heart showed that treated KO animals maintained normal ultrastructure and had less apoptotic events than the untreated KO animals. Additionally, treated KO animals had higher levels of total aconitase activity in the heart than in untreated animals, showing that protein replacement using TAT–FXN is capable of reconstituting Fe–S cluster-dependent enzymes. This also demonstrates that even though protein replacement with TAT–FXN was started later, it was still capable of rescuing the KO phenotype to extend the lifespan and survival.

There are substantial hurdles to delivering replacement proteins to mitochondria *in vivo* which are addressed by the use of cell-penetrant peptides. Mitochondria contain their own genome, ~16 500 bp in humans, which encodes 13 proteins and the transfer and ribosomal RNAs needed to translate them (80). The remaining hundreds of proteins needed for efficient mitochondrial function are encoded by the nuclear genome and imported in a multi-step energetic process from the cytosol (81). Proteins are essentially denatured as they

pass through the import apparatus and also do not contain post-translational modifications, such as glycosylation. As a result, mitochondria are well adapted to re-folding and processing proteins to generate active enzyme complexes. Thus, mitochondria present unique challenges to the development of therapies that address deficient or aberrant protein function, but also have unique features, such as the processing peptidases to remove a fusion protein tag like TAT, which can be leveraged to deliver an exogenous protein in designing a potential therapy.

Our approach took advantage of the fact that the MPP will proteolytically remove the MTS and any peptide sequence upstream of the MTS. This is important because if the TAT moiety remains attached, it is equally capable of transducing the fusion protein out of the mitochondria and cell (38). With processing by the MPP of the TAT leader sequence, the mitochondrial matrix ultimately sees the native mature FXN protein. The current data show that the precursor is ultimately cleaved at position FXN^{80-81} to yield the start of the mature peptide as ^{81}SGTLGH (29). Our results identified the intermediate cleavage site at ^{42}LRTDI when cleaved *in vitro* consistent with the description by Cavadini *et al*. (27). We were unable to generate *in vitro* sequence information by Edman degradation for the mature fragment consistent with earlier findings that the rate of the second cleavage *in vitro* is much slower. However, a mature fragment is generated and detected by western blotting, as shown in Figure 2B. This is in good agreement with the mature peptide predicted by Schmucker *et al*., as being FXN^{81-210} (29). Based on these data, it is logical to conclude that TAT–FXN is being properly recognized and cleaved by the native MPP.

The finding that the TAT–FXN-treated *Fxn-KO* animals had higher heart rates is significant. Neuron-specific enolase (NSE) is expressed in multiple regions of the heart including paraganglionic-like structures at high density near the upper third of the atrial septum (82,83). In addition, NSE has also been identified in multiple cell types, including nerve fibers, atrial adipose tissues, cardiomyocytes, intramyocardial paraganglia, which are closely related to myocardial fibers (82,84) and the conducting system of heart (85). Finally, the expression of NSE is developmentally regulated and is present in heart early during embryogenesis (62,63). Thus, NSE-Cre expression would be predicted to disrupt *Fxn* gene expression very early in heart and in multiple cell types, including innervations of the heart. Replacement of FXN would logically be expected to allow greater sympathetic response to cardiac innervation, which, when combined with improved diastolic filling of the ventricle, would result in higher CO.

It was interesting that the TAT–FXN-treated animals did not demonstrate complete rescue, even when treatment was begun on the third day of life. The TAT–FXN-treated *Fxn-KO* animals did not reach the same growth rate as the controls, nor live as long. Given that the promoter (NSE) driving the Cre expression is on in mid-embryogenesis (E10.5) in the brain (86,87) and heart (62,63), this also means that these animals had a congenital absence of FXN protein in selected tissues, and their disease phenotype had a substantial time to develop prior to birth. Earlier studies had shown that constitutive ablation of the *FXN* gene in the mouse was embryonic lethal emphasizing the importance of FXN protein early in development (60). Thus, one possibility for why complete rescue was not achieved is that substantial organ damage may already have occurred by the time treatment was initiated. This conclusion is supported by reports of children with the FRDA genotype who died very young from other causes prior to onset of symptoms and suggests that organ damage may be present from birth (88). Initiation of TAT–FXN prenatally in the mouse may, therefore, achieve greater rescue. Alternatively, there may be an inadequate FXN protein mass in critical tissues, such as the heart and brain, to achieve complete rescue, or else human FXN cannot substitute completely for mouse FXN. Finally, although no tissue immune response was identified, it is possible that humoral immune response eventually develops as has been reported for TAT-purine nucleoside phosphorylase (41), and may decrease effectiveness of injected TAT–FXN. As reported by Toro and Grunebaum, however, it was notable that even though the mouse mounted an immune response to TAT-purine nucleoside phosphorylase, the fusion protein was still quite effective at restoring enzyme activity.

It is also important to note that the animal model used in these studies is not an exact duplicate for either the phenotype or the genotype of patients with FRDA. Typically, patients will have $<$20% of normal FXN levels in affected tissues but not complete loss of FXN (89), and do not manifest overt symptoms until adolescence. In contrast, the mouse model used in these studies has a complete loss of FXN in those tissues expressing NSE and presents a very severe phenotype beginning at birth. These include tissues such as the brain, dorsal root ganglia, and other parts of the nervous and neuroendocrine systems, as well as the heart (85). However, using this model is a stringent test of the hypothesis that it is not necessary to replace FXN to normal levels to achieve a rescue of the phenotype. We were able to achieve an increased lifespan and restoration of enzymatic function in these animals with minimal dosing of TAT–FXN. Because enzymatically active TAT-fusion proteins have been shown to cross the blood-brain barrier (90–93) and our preliminary data have shown the presence of TAT–FXN in the brain of these treated animals (unpublished data), we would predict that future studies will show an improved neurologic function in treated animals. Studies of human FXN levels suggest that partial replacement of FXN may be enough to restore an adequate cellular function (94). If true, then partial replacement of FXN in FRDA patients with low, but measurable amounts of FXN may be adequate to restore normal cellular function. This would be especially important if tissue damage from the loss of FXN is cumulative and would justify early screening to initiate treatment(s).

METHODS AND MATERIALS

Detailed Methods and Materials are contained within the Supplementary Material.

TAT–FXN cDNA construction, protein expression and purification

The cDNA for human precursor FXN (GenBank accession NM_000144) was obtained from Invitrogen (clone ID

5300379). The sequence encoding the start site of the precursor FXN cDNA was amplified by PCR using oligonucleotides containing an *Nco*I restriction site at the start site N terminus (Forward: 5′-GGAGCACCATGGGGACTCTC-3′), and an *Eco*RI site in the reverse primer (Reverse: 5′-TAATGAATT CGGGGTCTTGGCCT-3′). The final product changed the N terminus tryptophan to a glycine, and was cloned in-frame into the *Nco*I–*Eco*RI sites of a bacterial expression vector containing the TAT sequence at the N terminus along with a 6× His tag at the N terminus to allow affinity purification (a gift from the Steve Dowdy lab, Washington University). The complete His–TAT–FXN cDNA construct (termed TAT–FXN) was transformed into BL21(DE3)pLysE cells for expression. The soluble fraction from expression was purified using nickel affinity chromatography, and exchanged into PBS for injection into animals. The TAT–mMDH–eGFP and TAT–GFP fusion proteins were expressed and purified as described previously (38) with minor modifications.

Expression and purification of mitochondrial processing peptidase

Plasmids containing the coding sequences of the mature α-MPP and β-MPP for the yeast were a kind gift from Drs. Jiri Adamec and Henry Weiner (both of Purdue University) and have been described as pETYA and pETYB, respectively (44). Both plasmids were subcloned into the pET-19b vector for expression and purification using a His affinity tag, and transformed into BL21(DE3) cells for expression and purification by nickel affinity chromatography.

Sequencing of TAT-fusion proteins

TAT-fusion proteins were incubated with MPP in a 1:1 ratio (e.g. 1 μg MPP total protein with 1 μg TAT–FXN total protein) at 37°C in a modified Factor XA cleavage buffer (20 mM Tris, pH 7.7, 1 mM $CaCl_2$, 50 mM NaCl, and 1 mM β-mercaptoethanol). Reaction products were separated by SDS–PAGE, transferred to Immobilon membranes and sequenced at the Iowa State University Protein Facility. Sequences obtained by Edman Degradation were compared with published sequences for intermediate and mature forms of human FXN (27) and rat mMDH (95,96).

Fluorescent labeling of TAT–FXN and localization in mitochondria

TAT–FXN was labeled with 5-IAF. Labeled protein was separated from unreacted salts on a PD-10 column with buffer exchange into PBS. FRDA fibroblasts were treated with 10 μg/ml of fluorescein-labeled TAT–FXN for 3 h, and then incubated with fresh media without labeled TAT–FXN for 120 h. At the time of microscopy, the cells were incubated with 200 nM of the mitochondrial dye CMXRos for 30 min at 37°C and imaged live on a Bio-Rad MRC-1024 laser scanning confocal inverted microscope.

Iron-binding activity of TAT–FXN protein in cell-free system

An aliquot of 5 μM each of ferrous sulfate and HQ (Fe/HQ) was incubated with PBS in the presence and in the absence of TAT–FXN (20, 40 μg/ml), or BSA (20 μg/ml) (negative control). An aliquot of 5 μM of DCHF-DA was hydrolyzed to DCHF by adding 200 μM NaOH and incubating the mixture in the dark for 30 min on ice. After 30 min, 250 μM of NaH_2PO_4 was added to neutralize the excess NaOH. An aliquot of 10 μl of this DCHF mixture was added to 200 μl of the reaction mixture to obtain 0.25 μM DCHF in the final assay. The fluorescence of DCF was measured at excitation wavelength of 485 nm and emission wavelength of 530 nm on a SpectraMax 340pc microplate spectrophotometer. As a positive control, an incubation containing 100 μM of EDTA as an iron chelator was performed to evaluate the role of iron in the oxidative mechanism of HQ.

Rescue of FRDA fibroblasts from oxidative stress by TAT–FXN

FRDA fibroblasts, and fibroblasts from a healthy age- and sex-matched control, were treated with and without TAT–FXN (20 and 40 μg/ml), or an equal volume of carrier fluid (PBS) as a negative control for 5 h, washed with PBS and then cultured overnight in culture media. The cells were then washed twice with PBS followed by the addition of Fe/HQ (5 μM of each component) in culture media for 5 h as an oxidant stress. Control cells were not treated with Fe/HQ. Following the 5 h treatment, cells were photographed under light microscopy for evidence of cytotoxicity.

Caspase-3 determination in TAT–FXN-treated FRDA fibroblasts

FRDA and age-/sex-matched control fibroblast cells were treated with and without TAT–FXN (20 and 40 μg/ml). After incubation, the cells were washed twice with PBS and treated with and without Fe/HQ (5 μM each component) in culture media for 3.5 h. After the plates were washed with PBS, the cells were scraped from the plate in 1 ml PBS, centrifuged and the cell pellet was mixed in cell lysis buffer per the manufacturer's instructions. The protein content of each sample was estimated and 750 μg of protein from each sample condition was loaded in a 96 black well, flat bottom, polystyrene assay plate and caspase-3 levels in each condition were quantified using the fluorescent substrate, 7-amino-4-methylcoumarin, at an excitation wavelength of 342 nm and emission wavelength of 441 nm.

FXN conditional KO animals, dosing and survival analysis

All animal protocols were approved by the Institutional Animal Care and Use Committee at Indiana University School of Medicine. Mice were bred for conditional deletion of the *Fxn* gene as described with minor modifications (33,87). Briefly, NSE-Cre mice were crossed with mice homozygous for a conditional allele of *Frda* ($Frda^{L3/L3}$) to generate mice heterozygous for the conditional allele

carrying theNSE-Cre transgene (*Frda*$^{L3/+}$:NSE-Cre). These *Frda*$^{L3/+}$:NSE-Cre mice were then crossed with *Frda*$^{L3/L3}$ mice to generate the final genotype with deletion of the *Fxn* gene in tissues expressing NSE. Genotyping of these animals was performed using oligonucleotide primers as described by Puccio *et al*. (33). Mice were dosed according to body weight with a total volume of ~20 μl/g of weight given IP. The dose interval was based on the published $T_{1/2}$ of 50 h for FXN (97). Survival curves for the mice were calculated using the Kaplan–Meier curve as described previously (64).

Electron microscopy

Tissue sections (~1–2 mm^3 volume) were fixed in modified Karnovsky's solution with 2% paraformaldehyde/2% glutaraldehyde in 0.1 M phosphate buffer, with post fixation in 1% osmium tetroxide in phosphate buffer for 1 h. The tissues were embedded in resin for sectioning. Sections were imaged on a Tecnai G2 12 Bio Twin transmission electron microscope at 80 kV at the Electron Microscopy Center of Indiana University School of Medicine.

Histology

Hearts were cryoprotected in 30% sucrose, embedded and sectioned at 6 μm thickness using standard techniques. Five transverse sections from each heart, sampled from the midpoint between the apex and base, were post-fixed in 4% paraformaldehyde and screened for anti-activated caspase-3 immune-reactivity, followed by a horseradish peroxidase-conjugated secondary antibody. The signal was visualized with a diaminobenzidine reaction as described previously (98).

Echocardiography

Control littermates, and *Fxn-KO* animals treated with, or without TAT–FXN, underwent echocardiography at 10–14d after initiation of injections with TAT–FXN in the KO-treated group. A 40 MHz hand-held mechanical transducer containing both imaging (B-mode) and Doppler transducers with a frame rate of 34 Hz was used to image the heart in multiple views as described previously (99). VisualSonics software (Version 2.3.2) was used to calculate ejection and shortening fractions, stroke volume, ventricular dimensions, and interpret the Doppler interrogation of mitral and aortic valve flow.

Aconitase activity

Aconitase-specific activity was measured in whole heart homogenates of ventricular tissues based on the downstream generation of NADPH. Briefly, whole heart was homogenized on ice and the NADPH change was measured via the absorbance at 340 nm using the end-point method on the Spectramax M5. Rates of conversion were normalized to total protein to generate specific activity.

Statistical analysis

All calculations, analyses and graphs were performed using SigmaPlot version 12.0 (Systat Software, Inc.). Data are presented as mean (±SD) unless otherwise indicated. Statistical comparisons between the two groups were made using Student's *t*-test with Mann–Whitney rank-sum test if the groups failed the normality test (Shapiro–Wilk), or equal variance test for normalized data. For comparisons between more than two groups, ANOVA and the Holm–Sidak method for multiple pairwise comparisons were used unless otherwise noted in the text. A *P*-value of <0.05 was considered to be significant.

SUPPLEMENTARY MATERIAL

Supplementary Material is available at *HMG* online.

ACKNOWLEDGEMENTS

We are deeply grateful to the Friedreich's Ataxia Research Alliance, and to Drs. Michel Koenig and Hélène Puccio for helpful discussions and mice. We are also grateful to Gregg Wagner and Kyle Martin for constructive criticism and review, and to Caroline Miller at the Electron Microscopy Center for expert ultrastructural imaging.

Conflict of Interest statement. None declared.

FUNDING

This work was supported by grants from the National Institutes of Health (R21NS 052198A1 and P01HL 085098A1 to R.M.P.); the American Heart Association (0855646G to R.M.P.); the Kyle Bryant award from the Friedreich's Ataxia Research Alliance (to R.M.P.); and the Federación de Ataxias de España (to R.M.P.). A sponsored research agreement with Shire Pharmaceuticals (Human Genetic Therapies unit, Cambridge, MA, USA) to R.M.P. supported part of the survival analysis.

REFERENCES

1. Harding, A.E. (1981) Friedreich's ataxia: a clinical and genetic study of 90 families with an analysis of early diagnostic criteria and intrafamilial clustering of clinical features. *Brain*, **104**, 589–620.
2. Malo, S., Latour, Y., Cote, M., Geoffroy, G., Lemieux, B. and Barbeau, A. (1976) Electrocardiographic and vectocardiographic findings in Friedreich's ataxia. *Can. J. Neurol. Sci.*, **3**, 323–328.
3. Tsou, A.Y., Paulsen, E.K., Lagedrost, S.J., Perlman, S.L., Mathews, K.D., Wilmot, G.R., Ravina, B., Koeppen, A.H. and Lynch, D.R. (2011) Mortality in friedreich ataxia. *J. Neurol. Sci.*, **307**, 46–49.
4. Schols, L., Amoiridis, G., Przuntek, H., Frank, G., Epplen, J.T. and Epplen, C. (1997) Friedreich's ataxia. Revision of the phenotype according to molecular genetics. *Brain*, **120** (Pt 12), 2131–2140.
5. Filla, A., De Michele, G., Marconi, R., Bucci, L., Carillo, C., Castellano, A.E., Iorio, L., Kniahynicki, C., Rossi, F. and Campanella, G. (1992) Prevalence of hereditary ataxias and spastic paraplegias in Molise, a region of Italy. *J. Neurol.*, **239**, 351–353.
6. Romeo, G., Menozzi, P., Ferlini, A., Fadda, S., Di Donato, S., Uziel, G., Lucci, B., Capodaglio, L., Filla, A. and Campanella, G. (1983) Incidence of Friedreich ataxia in Italy estimated from consanguineous marriages. *Am. J. Hum. Genet.*, **35**, 523–529.
7. Skre, H. (1975) Friedreich's ataxia in Western Norway. *Clin. Genet.*, **7**, 287–298.

8. Epplen, C., Epplen, J.T., Frank, G., Miterski, B., Santos, E.J. and Schols, L. (1997) Differential stability of the (GAA)n tract in the Friedreich ataxia (STM7) gene. *Hum. Genet.*, **99**, 834–836.
9. Pandolfo, M. (2008) Friedreich ataxia. *Arch. Neurol.*, **65**, 1296–1303.
10. Patel, P.I. and Isaya, G. (2001) Friedreich ataxia: from GAA triplet-repeat expansion to frataxin deficiency. *Am. J. Hum. Genet.*, **69**, 15–24.
11. Gacy, A.M., Goellner, G.M., Spiro, C., Chen, X., Gupta, G., Bradbury, E.M., Dyer, R.B., Mikesell, M.J., Yao, J.Z., Johnson, A.J. *et al.* (1998) GAA instability in Friedreich's Ataxia shares a common, DNA-directed and intraallelic mechanism with other trinucleotide diseases. *Mol. Cell.*, **1**, 583–593.
12. Sakamoto, N., Ohshima, K., Montermini, L., Pandolfo, M. and Wells, R.D. (2001) Sticky DNA, a self-associated complex formed at long GAA*TTC repeats in intron 1 of the frataxin gene, inhibits transcription. *J. Biol. Chem.*, **276**, 27171–27177.
13. Herman, D., Jenssen, K., Burnett, R., Soragni, E., Perlman, S.L. and Gottesfeld, J.M. (2006) Histone deacetylase inhibitors reverse gene silencing in Friedreich's ataxia. *Nat. Chem. Biol.*, **2**, 551–558.
14. Montermini, L., Richter, A., Morgan, K., Justice, C.M., Julien, D., Castellotti, B., Mercier, J., Poirier, J., Capozzoli, F., Bouchard, J.P. *et al.* (1997) Phenotypic variability in Friedreich ataxia: role of the associated GAA triplet repeat expansion. *Ann. Neurol.*, **41**, 675–682.
15. Filla, A., De Michele, G., Cavalcanti, F., Pianese, L., Monticelli, A., Campanella, G. and Cocozza, S. (1996) The relationship between trinucleotide (GAA) repeat length and clinical features in Friedreich ataxia. *Am. J. Hum. Genet.*, **59**, 554–560.
16. Zhang, Y., Lyver, E.R., Knight, S.A., Pain, D., Lesuisse, E. and Dancis, A. (2006) Mrs3p, Mrs4p, and frataxin provide iron for Fe–S cluster synthesis in mitochondria. *J. Biol. Chem.*, **281**, 22493–22502.
17. Huang, M.L., Becker, E.M., Whitnall, M., Rahmanto, Y.S., Ponka, P. and Richardson, D.R. (2009) Elucidation of the mechanism of mitochondrial iron loading in Friedreich's ataxia by analysis of a mouse mutant. *Proc. Natl Acad. Sci. USA*, **106**, 16381–16386.
18. Yoon, T. and Cowan, J.A. (2004) Frataxin-mediated iron delivery to ferrochelatase in the final step of heme biosynthesis. *J. Biol. Chem.*, **279**, 25943–25946.
19. Correia, A.R., Wang, T., Craig, E.A. and Gomes, C.M. (2010) Iron-binding activity in yeast frataxin entails a trade off with stability in the alpha1/beta1 acidic ridge region. *Biochem. J.*, **426**, 197–203.
20. Tsai, C.L. and Barondeau, D.P. (2010) Human frataxin is an allosteric switch that activates the Fe–S cluster biosynthetic complex. *Biochemistry*, **49**, 9132–9139.
21. Stemmler, T.L., Lesuisse, E., Pain, D. and Dancis, A. (2010) Frataxin and mitochondrial FeS cluster biogenesis. *J. Biol. Chem.*, **285**, 26737–26743.
22. Schmucker, S., Martelli, A., Colin, F., Page, A., Wattenhofer-Donze, M., Reutenauer, L. and Puccio, H. (2011) Mammalian frataxin: an essential function for cellular viability through an interaction with a preformed ISCU/NFS1/ISD11 iron–sulfur assembly complex. *PLoS One*, **6**, e16199.
23. Rotig, A., de, L.P., Chretien, D., Foury, F., Koenig, M., Sidi, D., Munnich, A. and Rustin, P. (1997) Aconitase and mitochondrial iron–sulphur protein deficiency in Friedreich ataxia. *Nat. Genet.*, **17**, 215–217.
24. Lodi, R., Cooper, J.M., Bradley, J.L., Manners, D., Styles, P., Taylor, D.J. and Schapira, A.H. (1999) Deficit of in vivo mitochondrial ATP production in patients with Friedreich ataxia. *Proc. Natl Acad. Sci. USA*, **96**, 11492–11495.
25. Lodi, R., Rajagopalan, B., Blamire, A.M., Cooper, J.M., Davies, C.H., Bradley, J.L., Styles, P. and Schapira, A.H. (2001) Cardiac energetics are abnormal in Friedreich ataxia patients in the absence of cardiac dysfunction and hypertrophy: an in vivo 31P magnetic resonance spectroscopy study. *Cardiovasc. Res.*, **52**, 111–119.
26. Gakh, O., Cavadini, P. and Isaya, G. (2002) Mitochondrial processing peptidases. *Biochim. Biophys. Acta*, **1592**, 63–77.
27. Cavadini, P., Adamec, J., Taroni, F., Gakh, O. and Isaya, G. (2000) Two-step processing of human frataxin by mitochondrial processing peptidase. Precursor and intermediate forms are cleaved at different rates. *J. Biol. Chem.*, **275**, 41469–41475.
28. Condo, I., Ventura, N., Malisan, F., Rufini, A., Tomassini, B. and Testi, R. (2007) In vivo maturation of human frataxin. *Hum. Mol. Genet.*, **16**, 1534–1540.
29. Schmucker, S., Argentini, M., Carelle-Calmels, N., Martelli, A. and Puccio, H. (2008) The in vivo mitochondrial two-step maturation of human frataxin. *Hum. Mol. Genet.*, **17**, 3521–3531.
30. Richardson, D.R. (2003) Friedreich's ataxia: iron chelators that target the mitochondrion as a therapeutic strategy? *Expert. Opin. Investig. Drugs*, **12**, 235–245.
31. Jauslin, M.L., Meier, T., Smith, R.A. and Murphy, M.P. (2003) Mitochondria-targeted antioxidants protect Friedreich ataxia fibroblasts from endogenous oxidative stress more effectively than untargeted antioxidants. *FASEB J.*, **17**, 1972–1974.
32. Hart, P.E., Lodi, R., Rajagopalan, B., Bradley, J.L., Crilley, J.G., Turner, C., Blamire, A.M., Manners, D., Styles, P., Schapira, A.H. *et al.* (2005) Antioxidant treatment of patients with Friedreich ataxia: four-year follow-up. *Arch. Neurol.*, **62**, 621–626.
33. Puccio, H., Simon, D., Cossee, M., Criqui-Filipe, P., Tiziano, F., Melki, J., Hindelang, C., Matyas, R., Rustin, P. and Koenig, M. (2001) Mouse models for Friedreich ataxia exhibit cardiomyopathy, sensory nerve defect and Fe–S enzyme deficiency followed by intramitochondrial iron deposits. *Nat. Genet.*, **27**, 181–186.
34. Schwarze, S.R., Ho, A., Vocero-Akbani, A. and Dowdy, S.F. (1999) In vivo protein transduction: delivery of a biologically active protein into the mouse. *Science*, **285**, 1569–1572.
35. Del Gaizo-Moore, V., MacKenzie, J.A. and Payne, R.M. (2003) Targeting proteins to mitochondria using TAT. *Mol. Genet. Metab*, **80**, 170–180.
36. Zhang, X.Y., Dinh, A., Cronin, J., Li, S.C. and Reiser, J. (2008) Cellular uptake and lysosomal delivery of galactocerebrosidase tagged with the HIV Tat protein transduction domain. *J. Neurochem.*, **104**, 1055–1064.
37. Jensen, K.D., Nori, A., Tijerina, M., Kopeckova, P. and Kopecek, J. (2003) Cytoplasmic delivery and nuclear targeting of synthetic macromolecules. *J. Control. Release*, **87**, 89–105.
38. Del Gaizo, V. and Payne, R.M. (2003) A novel TAT-Mitochondrial signal sequence fusion protein is processed, stays in mitochondria, and crosses the placenta. *Mol. Ther.*, **7**, 720–730.
39. Mishra, A., Lai, G.H., Schmidt, N.W., Sun, V.Z., Rodriguez, A.R., Tong, R., Tang, L., Cheng, J., Deming, T.J., Kamei, D.T. *et al.* (2011) Translocation of HIV TAT peptide and analogues induced by multiplexed membrane and cytoskeletal interactions. *Proc. Natl. Acad. Sci. U.S.A.*, **108**, 16883–16888.
40. Rapoport, M., Salman, L., Sabag, O., Patel, M.S. and Lorberboum-Galski, H. (2011) Successful TAT-mediated enzyme replacement therapy in a mouse model of mitochondrial E3 deficiency. *J. Mol. Med.*, **89**, 161–170.
41. Toro, A. and Grunebaum, E. (2006) TAT-mediated intracellular delivery of purine nucleoside phosphorylase corrects its deficiency in mice. *J. Clin. Invest.*, **116**, 2717–2726.
42. Pendergrass, W., Wolf, N. and Poot, M. (2004) Efficacy of MitoTracker Green and CMXrosamine to measure changes in mitochondrial membrane potentials in living cells and tissues. *Cytometry A*, **61**, 162–169.
43. Poot, M., Zhang, Y.Z., Kramer, J.A., Wells, K.S., Jones, L.J., Hanzel, D.K., Lugade, A.G., Singer, V.L. and Haugland, R.P. (1996) Analysis of mitochondrial morphology and function with novel fixable fluorescent stains. *J. Histochem. Cytochem.*, **44**, 1363–1372.
44. Adamec, J., Gakh, O., Spizek, J. and Kalousek, F. (1999) Complementation between mitochondrial processing peptidase (MPP) subunits from different species. *Arch. Biochem. Biophys.*, **370**, 77–85.
45. Chu, T.W., Eftime, R., Sztul, E. and Strauss, A.W. (1989) Synthetic transit peptides inhibit import and processing of mitochondrial precursor proteins. *J. Biol. Chem.*, **264**, 9552–9558.
46. Sztul, E.S., Chu, T.W., Strauss, A.W. and Rosenberg, L.E. (1988) Import of the malate dehydrogenase precursor by mitochondria. Cleavage within leader peptide by matrix protease leads to formation of intermediate-sized form. *J. Biol. Chem.*, **263**, 12085–12091.
47. Isaya, G., Kalousek, F., Fenton, W.A. and Rosenberg, L.E. (1991) Cleavage of precursors by the mitochondrial processing peptidase requires a compatible mature protein or an intermediate octapeptide. *J. Cell. Biol.*, **113**, 65–76.
48. Lu, C. and Cortopassi, G. (2007) Frataxin knockdown causes loss of cytoplasmic iron–sulfur cluster functions, redox alterations and induction of heme transcripts. *Arch. Biochem. Biophys.*, **457**, 111–122.
49. Bulteau, A.L., O'Neill, H.A., Kennedy, M.C., Ikeda-Saito, M., Isaya, G. and Szweda, L.I. (2004) Frataxin acts as an iron chaperone protein to modulate mitochondrial aconitase activity. *Science*, **305**, 242–245.
50. Mordente, A., Martorana, G.E., Minotti, G. and Giardina, B. (1998) Antioxidant properties of 2,3-dimethoxy-5-methyl-6-(10-hydroxydecyl)-1,4-benzoquinone (idebenone). *Chem. Res. Toxicol.*, **11**, 54–63.

51. Gillner, M., Moore, G.S., Cederberg, H. and Gustafsson, K. (1994) *Hydroquinone (environmental Health Criteria, No 157)*. World Health Organization, Geneva, Switzerland.
52. Pastore, C., Franzese, M., Sica, F., Temussi, P. and Pastore, A. (2007) Understanding the binding properties of an unusual metal-binding protein–a study of bacterial frataxin. *Febs J*, **274**, 4199–4210.
53. Radisky, D.C., Babcock, M.C. and Kaplan, J. (1999) The yeast frataxin homologue mediates mitochondrial iron efflux. Evidence for a mitochondrial iron cycle. *J. Biol. Chem.*, **274**, 4497–4499.
54. Foury, F. and Cazzalini, O. (1997) Deletion of the yeast homologue of the human gene associated with Friedreich's ataxia elicits iron accumulation in mitochondria. *FEBS Lett.*, **411**, 373–377.
55. Wong, A., Yang, J., Cavadini, P., Gellera, C., Lonnerdal, B., Taroni, F. and Cortopassi, G. (1999) The Friedreich's ataxia mutation confers cellular sensitivity to oxidant stress which is rescued by chelators of iron and calcium and inhibitors of apoptosis. *Hum. Mol. Genet.*, **8**, 425–430.
56. Lin, F. and Girotti, A.W. (1997) Elevated ferritin production, iron containment, and oxidant resistance in hemin-treated leukemia cells. *Arch. Biochem. Biophys.*, **346**, 131–141.
57. Oubidar, M., Marie, C., Mossiat, C. and Bralet, J. (1996) Effects of increasing intracellular reactive iron level on cardiac function and oxidative injury in the isolated rat heart. *J. Mol. Cell. Cardiol.*, **28**, 1769–1776.
58. Sogabe, K., Roeser, N.F., Venkatachalam, M.A. and Weinberg, J.M. (1996) Differential cytoprotection by glycine against oxidant damage to proximal tubule cells. *Kidney Int.*, **50**, 845–854.
59. Balla, G., Vercellotti, G.M., Eaton, J.W. and Jacob, H.S. (1990) Iron loading of endothelial cells augments oxidant damage. *J. Lab. Clin. Med.*, **116**, 546–554.
60. Cossee, M., Puccio, H., Gansmuller, A., Koutnikova, H., Dierich, A., LeMeur, M., Fischbeck, K., Dolle, P. and Koenig, M. (2000) Inactivation of the Friedreich ataxia mouse gene leads to early embryonic lethality without iron accumulation. *Hum. Mol. Genet.*, **9**, 1219–1226.
61. Cinato, E., Mirotsou, M. and Sablitzky, F. (2001) Cre-mediated transgene activation in the developing and adult mouse brain. *Genesis*, **31**, 118–125.
62. El Sharaby, A.A., Egerbacher, M., Hammoda, A.K. and Bock, P. (2001) Immunohistochemical demonstration of Leu-7 (HNK-1), Neurone-specific Enolase (NSE) and Protein-Gene Peptide (PGP) 9.5 in the developing camel (Camelus dromedarius) heart. *Anat. Histol. Embryol.*, **30**, 321–325.
63. Semba, R., Asano, T. and Kato, K. (1990) Physiological expression of neural marker proteins in the heart of young rats. *Brain Res. Dev. Brain Res.*, **54**, 217–220.
64. Bland, J.M. and Altman, D.G. (2004) The logrank test. *Br. Med. J.*, **328**, 1073.
65. Patel, A.L., Engstrom, J.L., Meier, P.P. and Kimura, R.E. (2005) Accuracy of methods for calculating postnatal growth velocity for extremely low birth weight infants. *Pediatrics*, **116**, 1466–1473.
66. Stehling, O., Elsasser, H.P., Bruckel, B., Muhlenhoff, U. and Lill, R. (2004) Iron–sulfur protein maturation in human cells: evidence for a function of frataxin. *Hum. Mol. Genet.*, **13**, 3007–3015.
67. Whitnall, M., Rahmanto, Y.S., Sutak, R., Xu, X., Becker, E.M., Mikhael, M.R., Ponka, P. and Richardson, D.R. (2008) The MCK mouse heart model of Friedreich's ataxia: alterations in iron-regulated proteins and cardiac hypertrophy are limited by iron chelation. *Proc. Natl Acad. Sci. USA*, **105**, 9757–9762.
68. Seznec, H., Simon, D., Bouton, C., Reutenauer, L., Hertzog, A., Golik, P., Procaccio, V., Patel, M., Drapier, J.C., Koenig, M. *et al.* (2005) Friedreich ataxia: the oxidative stress paradox. *Hum. Mol. Genet.*, **14**, 463–474.
69. Martelli, A., Wattenhofer-Donze, M., Schmucker, S., Bouvet, S., Reutenauer, L. and Puccio, H. (2007) Frataxin is essential for extramitochondrial Fe–S cluster proteins in mammalian tissues. *Hum. Mol. Genet.*, **16**, 2651–2658.
70. Lill, R. and Muhlenhoff, U. (2008) Maturation of iron–sulfur proteins in eukaryotes: mechanisms, connected processes, and diseases. *Annu. Rev. Biochem.*, **77**, 669–700.
71. Noble, R.J. and Nutter, D.O. (1970) The demonstration of alternating contractile state in pulsus alternans. *J. Clin. Invest.*, **49**, 1166–1177.
72. Ho, C.Y. (2007) Echocardiographic assessment of diastolic function. In Solomon, S.D. and Bulwer, B.E. (eds), *Essential Echocardiography: A Practical Handbook*. Humana Press, New York, pp. 119–131.
73. Dutka, D.P., Donnelly, J.E., Palka, P., Lange, A., Nunez, D.J. and Nihoyannopoulos, P. (2000) Echocardiographic characterization of cardiomyopathy in Friedreich's ataxia with tissue Doppler echocardiographically derived myocardial velocity gradients. *Circulation*, **102**, 1276–1282.
74. Laguens, R.P. and Gomez-Dumm, C.L. (1967) Fine structure of myocardial mitochondria in rats after exercise for one-half to two hours. *Circ. Res.*, **21**, 271–279.
75. Laguens, R.P., Weinschelbaun, R. and Favaloro, R. (1979) Ultrastructural and morphometric study of the human heart muscle cell in acute coronary insufficiency. *Hum. Pathol.*, **10**, 695–705.
76. Zhu, W., Soonpaa, M.H., Chen, H., Shen, W., Payne, R.M., Liechty, E.A., Caldwell, R.L., Shou, W. and Field, L.J. (2009) Acute doxorubicin cardiotoxicity is associated with p53-induced inhibition of the mammalian target of rapamycin pathway. *Circulation*, **119**, 99–106.
77. Morvan, D., Komajda, M., Doan, L.D., Brice, A., Isnard, R., Seck, A., Lechat, P., Agid, Y. and Grosgogeat, Y. (1992) Cardiomyopathy in Friedreich's ataxia: a Doppler-echocardiographic study. *Eur. Heart. J.*, **13**, 1393–1398.
78. Mottram, P.M., Delatycki, M.B., Donelan, L., Gelman, J.S., Corben, L. and Peverill, R.E. (2011) Early changes in left ventricular long-axis function in Friedreich ataxia: relation with the FXN gene mutation and cardiac structural change. *J. Am. Soc. Echocardiogr.*, **24**, 782–789.
79. Regner, S.R., Lagedrost, S.J., Plappert, T., Paulsen, E.K., Friedman, L.S., Snyder, M.L., Perlman, S.L., Mathews, K.D., Wilmot, G.R., Schadt, K.A. *et al.* (2011) Analysis of Echocardiograms in a Large Heterogeneous Cohort of Patients with Friedreich Ataxia. *Am. J. Cardiol.* [Epub ahead of print].
80. Wallace, D.C. (1999) Mitochondrial diseases in man and mouse. *Science*, **283**, 1482–1488.
81. Neupert, W. and Herrmann, J.M. (2007) Translocation of proteins into mitochondria. *Annu. Rev. Biochem.*, **76**, 723–749.
82. Gobbi, H., Barbosa, A.J., Teixeira, V.P. and Almeida, H.O. (1991) Immunocytochemical identification of neuroendocrine markers in human cardiac paraganglion-like structures. *Histochemistry*, **95**, 337–340.
83. Pearce, J.M., Edwards, Y.H. and Harris, H. (1976) Human enolase isozymes: electrophoretic and biochemical evidence for three loci. *Ann. Hum. Genet.*, **39**, 263–276.
84. Skowasch, D., Jabs, A., Andrie, R., Dinkelbach, S., Luderitz, B. and Bauriedel, G. (2003) Presence of bone-marrow- and neural-crest-derived cells in intimal hyperplasia at the time of clinical in-stent restenosis. *Cardiovasc. Res.*, **60**, 684–691.
85. Haimoto, H., Takahashi, Y., Koshikawa, T., Nagura, H. and Kato, K. (1985) Immunohistochemical localization of gamma-enolase in normal human tissues other than nervous and neuroendocrine tissues. *Lab. Invest.*, **52**, 257–263.
86. Forss-Petter, S., Danielson, P.E., Catsicas, S., Battenberg, E., Price, J., Nerenberg, M. and Sutcliffe, J.G. (1990) Transgenic mice expressing beta-galactosidase in mature neurons under neuron-specific enolase promoter control. *Neuron*, **5**, 187–197.
87. Frugier, T., Tiziano, F.D., Cifuentes-Diaz, C., Miniou, P., Roblot, N., Dierich, A., Le, M.M. and Melki, J. (2000) Nuclear targeting defect of SMN lacking the C-terminus in a mouse model of spinal muscular atrophy. *Hum. Mol. Genet.*, **9**, 849–858.
88. Quercia, N., Somers, G.R., Halliday, W., Kantor, P.F., Banwell, B. and Yoon, G. (2010) Friedreich ataxia presenting as sudden cardiac death in childhood: clinical, genetic and pathological correlation, with implications for genetic testing and counselling. *Neuromuscul. Disord.*, **20**, 340–342.
89. Campuzano, V., Montermini, L., Lutz, Y., Cova, L., Hindelang, C., Jiralerspong, S., Trottier, Y., Kish, S.J., Faucheux, B., Trouillas, P. *et al.* (1997) Frataxin is reduced in Friedreich ataxia patients and is associated with mitochondrial membranes. *Hum. Mol. Genet.*, **6**, 1771–1780.
90. Ye, N., Liu, S., Lin, Y. and Rao, P. (2011) Protective effects of intraperitoneal injection of TAT-SOD against focal cerebral ischemia/reperfusion injury in rats. *Life Sciences*, **89**, 868–874.
91. Asoh, S., Ohsawa, I., Mori, T., Katsura, K., Hiraide, T., Katayama, Y., Kimura, M., Ozaki, D., Yamagata, K. and Ohta, S. (2002) Protection against ischemic brain injury by protein therapeutics. *Proc. Natl Acad. Sci. USA*, **99**, 17107–17112.
92. Cao, G., Pei, W., Ge, H., Liang, Q., Luo, Y., Sharp, F.R., Lu, A., Ran, R., Graham, S.H. and Chen, J. (2002) In vivo delivery of a Bcl-xL fusion protein containing the TAT protein transduction domain protects against ischemic brain injury and neuronal apoptosis. *J. Neurosci.*, **22**, 5423–5431.

93. Kim, D.W., Eum, W.S., Jang, S.H., Kim, S.Y., Choi, H.S., Choi, S.H., An, J.J., Lee, S.H., Lee, K.S., Han, K. *et al.* (2005) Transduced Tat-SOD fusion protein protects against ischemic brain injury. *Mol. Cells*, **19**, 88–96.
94. Tan, G., Chen, L.S., Lonnerdal, B., Gellera, C., Taroni, F.A. and Cortopassi, G.A. (2001) Frataxin expression rescues mitochondrial dysfunctions in FRDA cells. *Hum. Mol. Genet.*, **10**, 2099–2107.
95. Grant, P.M., Roderick, S.L., Grant, G.A., Banaszak, L.J. and Strauss, A.W. (1987) Comparison of the precursor and mature forms of rat heart mitochondrial malate dehydrogenase. *Biochemistry*, **26**, 128–134.
96. Grant, P.M., Tellam, J., May, V.L. and Strauss, A.W. (1986) Isolation and nucleotide sequence of a cDNA clone encoding rat mitochondrial malate dehydrogenase. *Nucleic Acids Res.*, **14**, 6053–6066.
97. Li, K., Besse, E.K., Ha, D., Kovtunovych, G. and Rouault, T.A. (2008) Iron-dependent regulation of frataxin expression: implications for treatment of Friedreich ataxia. *Hum. Mol. Genet.*, **17**, 2265–2273.
98. Nakajima, H., Nakajima, H.O., Tsai, S.C. and Field, L.J. (2004) Expression of mutant p193 and p53 permits cardiomyocyte cell cycle reentry after myocardial infarction in transgenic mice. *Circ. Res.*, **94**, 1606–1614.
99. Gao, X.M., Agrotis, A., Autelitano, D.J., Percy, E., Woodcock, E.A., Jennings, G.L., Dart, A.M. and Du, X.J. (2003) Sex hormones and cardiomyopathic phenotype induced by cardiac beta 2-adrenergic receptor overexpression. *Endocrinology*, **144**, 4097–4105.